



# BRNO UNIVERSITY OF TECHNOLOGY

VYSOKÉ UČENÍ TECHNICKÉ V BRNĚ

## FACULTY OF MECHANICAL ENGINEERING

FAKULTA STROJNÍHO INŽENÝRSTVÍ

## INSTITUTE OF PHYSICAL ENGINEERING

ÚSTAV FYZIKÁLNÍHO INŽENÝRSTVÍ

# MULTIPHOTON AND NON-LINEAR RAMAN MICROSCOPY THROUGH A MULTIMODE FIBRE

VÍCEFOTONOVÁ A NELINEÁRNÍ RAMANOVSKÁ MIKROSKOPIE SKRZ MULTIMODOVÉ VLÁKNO

## SHORT VERSION OF DOCTORAL THESIS

TEZE DIZERTAČNÍ PRÁCE

### AUTHOR

AUTOR PRÁCE

Ing. Tomáš Pikálek

### SUPERVISOR

ŠKOLITEL

prof. Mgr. Tomáš Čižmár, Ph.D.

BRNO 2023



## Summary

Multimode fibres have recently shown promise as miniature endoscopic probes for imaging deep inside brain tissue of mouse animal models with minimal damage. By employing wavefront shaping, the speckle pattern associated with coherent light propagation through a multimode fibre can be transformed into a tightly focused point, essentially turning the fibre into a miniature point-scanning device. Many microscopic techniques have been successfully implemented through a multimode fibre, and even in-vivo imaging has been demonstrated. This work extends the capabilities to label-free non-linear microscopy with chemical contrast using coherent anti-Stokes Raman scattering (CARS), which can potentially extend the use of multimode fibre endoscopes to clinical applications for, for example, tumour diagnosis. The main focus is the optimisations of the endoscopic system and the fibre probe to allow efficient focusing of pulsed light through multimode fibres, including dispersion control and thus allowing implementation of non-linear imaging techniques. The optimised setup is then employed to demonstrate CARS imaging of biologically relevant tissue, such as myelinated axons in a mouse brain, and chemical selectivity is verified by imaging polymer beads. In addition, multimodal CARS and two-photon excitation fluorescence (TPEF) imaging of fixed mouse tissue is demonstrated.

## Abstrakt

Multimodová vlákna je možné využít jako miniaturní endoskopy pro zobrazování hluboko uvnitř mozku myších zvířecích modelů s minimálním poškozením okolní tkáně. S využitím metod tvarování vlnoplochy je možné svazek vystupující z vlákna fokusovat do jediného bodu, a vytvořit tak miniaturní skenovací mikroskop. Různé mikroskopické zobrazovací metody již byly tímto způsobem implementovány, a to včetně několika in-vivo demonstrací. Tato práce se zabývá implementací zobrazování pomocí koherentního anti-Stokesova Ramanova rozptylu (CARS), nelineární metody umožňující zobrazování s chemickým kontrastem bez značení vzorku. Tato metoda má potenciální využití pro klinické aplikace například při diagnóze nádorů. Práce je zaměřena zejména na optimalizaci endoskopu a vláknových sond pro fokusaci světla z pulzních laserů včetně kontroly disperze s cílem umožnit nelineární zobrazování. Takto optimalizovaný systém je následně využit pro demonstraci zobrazování metodou CARS uvnitř tkáně (například lipidové dvojvrstvy buněčných membrán kolem axonů) a chemického kontrastu na polymerových kuličkách. Systém je též použit k demonstraci multimodálního zobrazování fixované myší tkáně kombinací CARS a dvoufotonové mikroskopie.

## Keywords

multimode fibre imaging, endoscopy, non-linear microscopy, two-photon excitation fluorescence (TPEF), coherent anti-Stokes Raman spectroscopy (CARS)

## Klíčová slova

zobrazování multimodovým vláknem, endoskopie, nelineární mikroskopie, dvoufotonová mikroskopie, koherentní anti-Stokesův Ramanův rozptyl

PIKÁLEK, Tomáš. *Multiphoton and non-linear Raman microscopy through a multimode fibre*. Brno, 2023. 34 pp. Short version of doctoral thesis. Brno University of Technology. Faculty of Mechanical Engineering. Supervisor Tomáš ČIŽMÁR.



# Contents

<b>Introduction</b>	<b>1</b>
<b>1. Wavelength-dependent behaviour of a fibre endoscope</b>	<b>3</b>
1.1. Setup for fibre characterisation . . . . .	3
1.2. Spatial light modulator dispersion compensation . . . . .	4
1.3. Bandwidth of multimode fibres . . . . .	6
1.4. Femtosecond laser focusing . . . . .	8
1.5. Spectral phase of the focused point . . . . .	8
1.6. Summary . . . . .	9
<b>2. Coherent anti-Stokes Raman scattering through fibre</b>	<b>11</b>
2.1. Optical setup . . . . .	11
2.2. Imaging of polymer beads . . . . .	12
2.3. Summary . . . . .	14
<b>3. Non-linear imaging using a femtosecond laser</b>	<b>17</b>
3.1. Optical setup . . . . .	17
3.2. Background suppression . . . . .	18
3.3. Focusing performance of composite probes . . . . .	20
3.4. Imaging . . . . .	22
3.5. Summary . . . . .	24
<b>Conclusions</b>	<b>27</b>
<b>References</b>	<b>29</b>



# Introduction

Scattering effects make biological tissue mostly opaque to light, limiting the maximal depth for optical imaging. For state-of-the-art multiphoton imaging techniques and brain tissue, the penetration depth can exceed several hundred of micrometres (for two-photon excitation fluorescence) or even a millimetre (for three-photon excitation) [1, 2].

While the development in focusing through complex media could overcome some of the scattering effects [3], the maximal imaging depth while maintaining subcellular resolution is still limited. Since other non-invasive imaging approaches, such as computed tomography or magnetic resonance imaging, do not allow for sufficient resolution, imaging deeper requires bringing the imaging instrument closer to the target area. Endoscopes are often used to reduce the damage to the surrounding tissue [4], typically based on fibre bundles [5] or graded-index (GRIN) lenses [6–9]. The diameter of such endoscopes starts at several hundreds of micrometres, making the impact on the tissue relatively large.

Advances in wavefront shaping have provided tools to transform a single multimode fibre into a miniature endoscope [10, 11]. The diameter of such fibre is typically in the range of  $100\mu\text{m}$ , and the numerical aperture of the fibre determines the spatial resolution of the endoscope. These properties make multimode fibres suitable for minimally invasive imaging deep inside sensitive tissue.

Many imaging techniques have been implemented a single multimode fibre, including in-vivo demonstrations [12–14]. As for non-linear imaging, two-photon excitation fluorescence (TPEF) has been shown [15–17]. The goal of this thesis is the implementation of coherent anti-Stokes Raman scattering (CARS) imaging through multimode fibre. This technique allows label-free imaging with chemical contrast [18]. CARS and other non-linear techniques like TPEF and second-harmonic generation (SHG) are essential tools for performing optical biopsies for diagnosing tumours and other diseases [19]. Thus, implementing CARS through a multimode fibre would pave the way towards clinical applications of multimode fibre endoscopes.

The short version of the thesis is divided into three chapters, corresponding to papers [20–22]. In the first chapter, a wavelength-dependent characterisation of the multimode fibre endoscope is performed. The results are then used in the second chapter to demonstrate coherent anti-Stokes Raman scattering imaging through the multimode fibre endoscope using a picosecond laser system, and in the third chapter, to demonstrate multimodal two-photon excitation fluorescence and coherent anti-Stokes Raman scattering imaging through a multimode fibre using a femtosecond laser system.

INTRODUCTION



# 1. Wavelength-dependent behaviour of a fibre endoscope

Implementing non-linear imaging, such as two-photon excitation fluorescence (TPEF), coherent anti-Stokes Raman scattering (CARS) or second-harmonic generation (SHG) imaging, through a multimode fibre puts several requirements on the endoscopic imaging system. In particular, it is necessary to focus light from pulsed lasers. Since the propagation of light through multimode fibres is wavelength dependent, the bandwidth of such fibres is limited, potentially limiting the ability to focus short pulses. In addition, the pulse length should be kept short and equal across the field of view, which might require employing dispersion compensation techniques. CARS imaging through a multimode fibre then puts additional demands on the endoscope. To implement CARS, two wavelengths separated by around  $3000\text{ cm}^{-1}$  must be focused simultaneously, ensuring a spatial and temporal overlap of both beams in the sample plane. It is also beneficial to be able to tune one (or both) of the two wavelengths in a small range (ideally about  $250\text{ cm}^{-1}$ , i.e.,  $\approx 15\text{ nm}$ ) to target different molecules (lipids, proteins and DNA, for example) without the necessity of repeating the calibration.

In previous research on non-linear imaging through a multimode fibre, out of the three mentioned methods, only TPEF imaging has been implemented [15–17, 23]. Focusing of pulsed lasers through multimode fibres has thus been demonstrated, nevertheless, the quality of the foci demonstrated typically did not match the one achievable with continuous-wave (CW) lasers during linear imaging using similar fibres, and no in-depth investigation of the differences between different fibres has been conducted. Thus, it is unclear how to choose a fibre for the endoscope and what modifications are required compared to a system used for linear imaging.

In this chapter, the multimode fibre endoscope is characterised in detail with an emphasis on the modifications necessary to fulfil the above-discussed requirements and allow efficient implementation of TPEF, CARS and SHG.

## 1.1. Setup for fibre characterisation

A simplified schematic drawing of the optical setup for multimode fibre characterisation is shown in Figure 1.1. Two different lasers could be coupled into the system. A tunable narrowband continuous-wave (CW) laser was used for most experiments presented in this chapter. Another laser used in this chapter was a tunable femtosecond laser.

The beam from the laser was expanded using a pair of lenses to significantly overfill the active area of a liquid crystal phase-only spatial light modulator (SLM). After diffracting off the SLM, the beam was Fourier transformed using a lens, allowing separation of the diffraction orders. The SLM created four beams with different ranges of spatial

## 1. WAVELENGTH-DEPENDENT BEHAVIOUR OF A FIBRE ENDOSCOPE

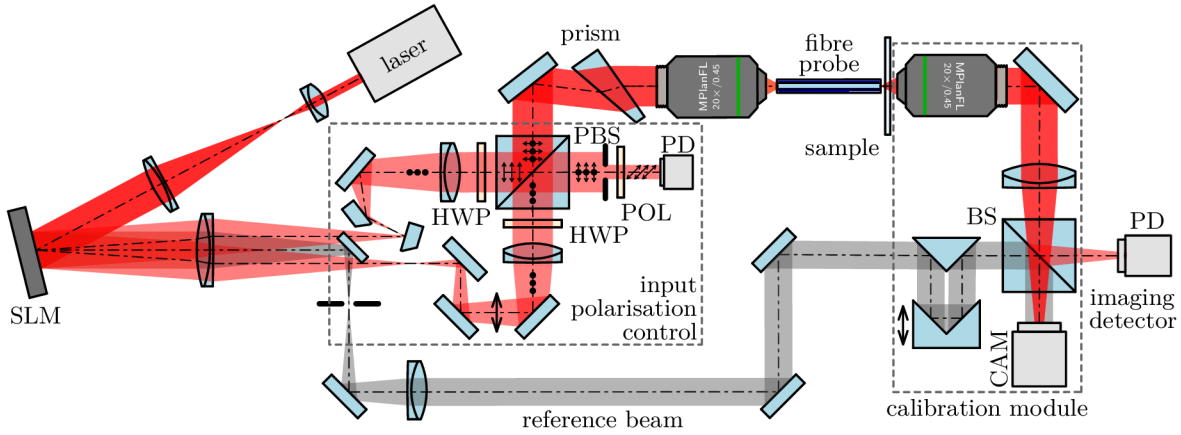


Figure 1.1: Simplified schematic drawing of the setup for multimode fibre endoscope characterisation. BS – non-polarising beamsplitter, CAM – camera, HWP – half-wave plate, SLM – spatial light modulator, PD – photodiode.

frequencies. The 0<sup>th</sup> order was always present and was not used for the experiments. The reference beam was isolated using an iris and collimated. After passing through a delay line, it was overlapped with the beam exiting the multimode fibre using a non-polarising beamsplitter. Another two beams created by the SLM (one for each input polarisation) were coupled into the multimode fibre. Both beams were first collimated. The polarisation of one of the beams was turned by 90° using an achromatic half-wave plate. Both beams were then overlapped using a polarising beamsplitter cube. By setting the relative phase and amplitude of these two beams on the SLM, the polarisation state at the input of the fibre could be locally controlled. The input polarisation control was essential when graded-index fibres were used. These, unlike step-index fibre, do not maintain circular polarisation. The relative phase between the two input polarisation beams was measured and stabilised during the imaging by passing the beams through a polariser with its axis oriented at 45° and monitoring the interference on a photodiode.

The holograms displayed on the SLM had a form of a sum of blazed diffraction gratings, which caused the position of the beams in the Fourier plane to be wavelength-dependent. To correct for this effect, a wedge prism could be placed in the beam before it was focused onto the multimode fibre using an objective.

The distal end of the multimode fibre was imaged onto a camera using an objective and a lens to characterise the light propagation through the fibre (measure its transmission matrix) and create a focused point at the distal end of the fibre. The image was then overlapped with the reference beam using the non-polarising beamsplitter cube. For imaging in transmission, an amplified photodetector was placed in the beam reflected off the beamsplitter.

### 1.2. Spatial light modulator dispersion compensation

The ability to tune the excitation wavelength after calibration is a valuable property for CARS imaging as it allows exciting different Raman shifts without the necessity to perform multiple calibrations. The fibre imaging system contained two elements that significantly changed the behaviour with wavelength. One of the elements was the SLM used in an off-axis configuration. The holograms displayed on the SLM had a form of sums of blazed diffraction gratings. Therefore, the diffraction angle changed when the

## 1.2. SPATIAL LIGHT MODULATOR DISPERSION COMPENSATION

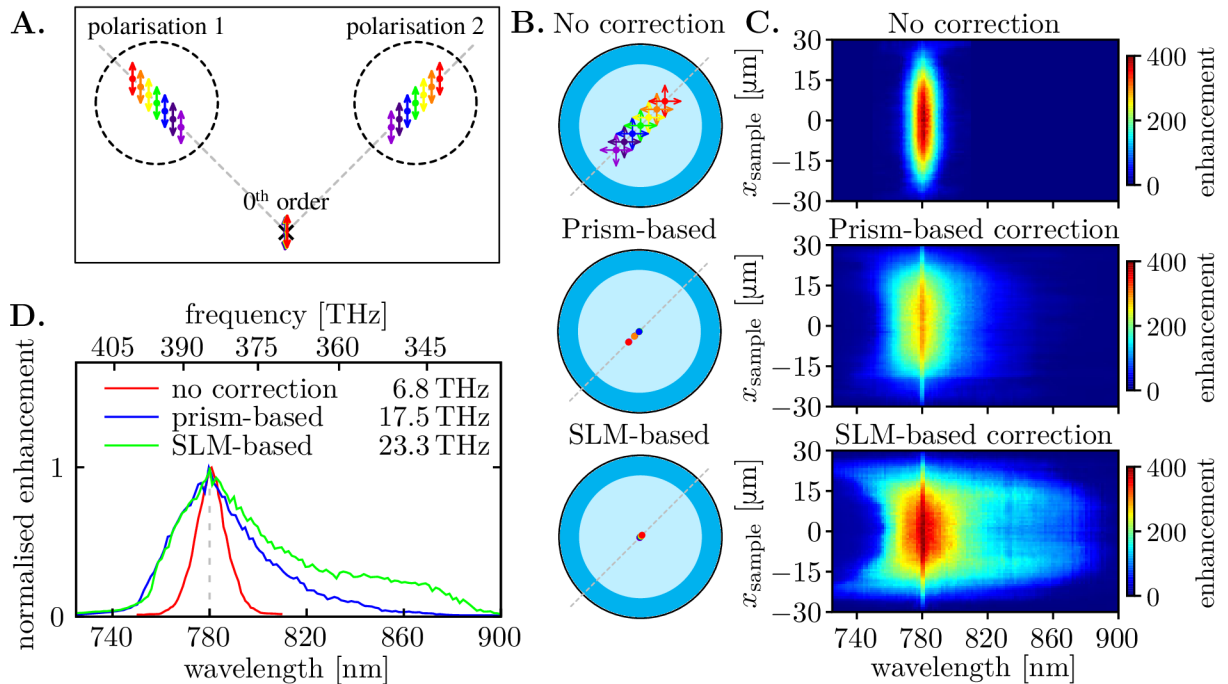


Figure 1.2: SLM dispersion compensation techniques. **A.** SLM Fourier plane. **B.** Fibre input facet for three situations. **C.** Measurement of the wavelength tuning range. **D.** Comparison for a point on axis.

wavelength changed, which changed the pattern projected to the proximal end of the multimode fibre (Figure 1.2A,B). This effect and methods for correcting the dispersion of the SLM is studied in this section. The second highly wavelength-dependent element was the multimode fibre itself, which is studied in Section 1.3.

One option for compensating for the wavelength-dependent behaviour of the SLM is to recalculate the hologram after the laser wavelength is changed to keep the diffraction angle constant. This method is referred to as the *SLM-based correction*. This correction was applicable only for one wavelength at a time; it could not be used to correct the dispersion for a broadband light. Another option for dispersion compensation involved placing another dispersive element in the beam path, like a prism [24]. A wedge prism was placed in a conjugate plane to the plane of the SLM (i.e., the SLM was imaged into the prism) to implement this correction in the endoscope. This method is referred to as the *prism-based correction*.

The performance of both methods for dispersion compensation is evaluated in Figure 1.2C,D. The fibre imaging system with a 50 mm long Prysmian DrakaElite fibre was calibrated at 780 nm. Afterwards, the wavelength of the laser was tuned. The quality of the focused points (in terms of intensity enhancement) across the field of view was evaluated for a range of wavelengths. When no correction was used, the wavelength tuning range was the lowest ( $\pm 7$  nm from the calibration wavelength). The prism-based correction increased the wavelength tuning range by a factor of about 2. The resulting tuning range of  $\pm 17$  nm from the calibration wavelength would be sufficient for CARS imaging of lipids and proteins. The SLM-based correction increased the tuning range by a factor of 3 to about  $\pm 24$  nm. However, in this case, the tuning range was likely limited not by the SLM, but rather by the bandwidth of the multimode fibre.

The effect of the SLM dispersion compensation was further demonstrated by imaging a 1951 USAF resolution test chart in Figure 1.3. The figure shows point spread functions

## 1. WAVELENGTH-DEPENDENT BEHAVIOUR OF A FIBRE ENDOSCOPE

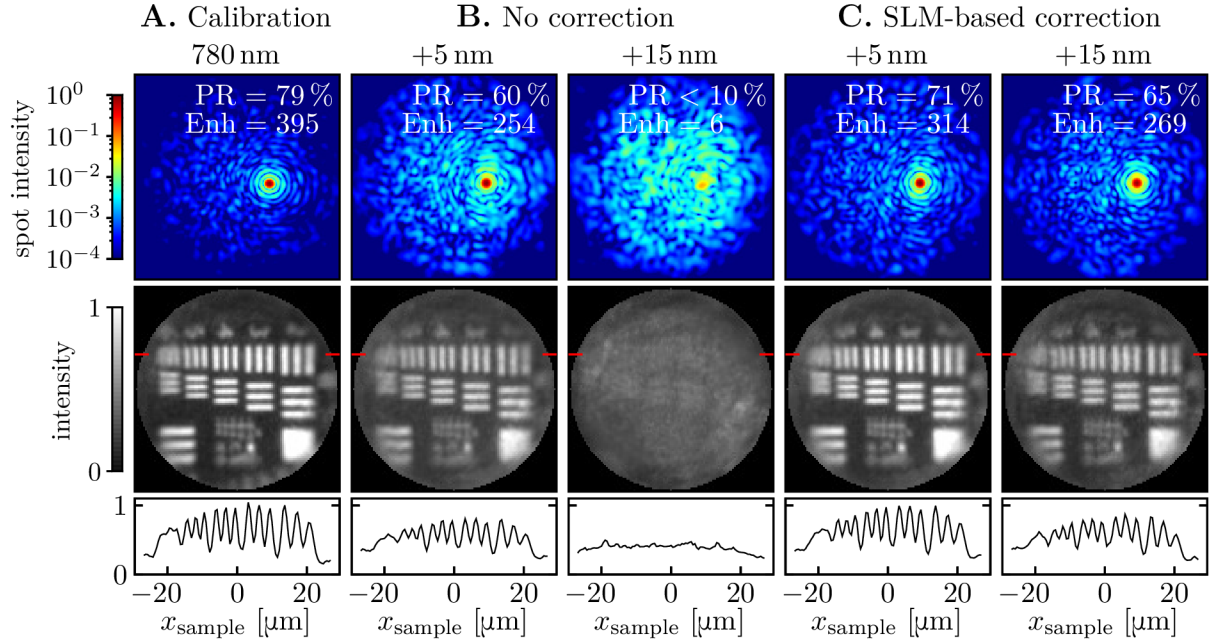


Figure 1.3: Demonstration of the effect of SLM dispersion compensation on imaging (group 8 of a 1951 USAF resolution test chart imaged in transmission). **A.** Point spread function and image at the calibration wavelength of 780 nm. PR is the power ratio, and Enh the intensity enhancement of the point. **B.**, **C.** Points and images after the wavelength was tuned.

after the wavelength was tuned from the calibration wavelength. These points were used for imaging the resolution test chart in transmission. With no correction, the contrast in the images dropped to near zero after a 15 nm wavelength change, as the power ratio (the fraction of the power at the distal end of the fibre contained in the focused point) of the point dropped significantly. When the SLM-based correction was used, the drop in the power ratio was slower, allowing imaging over a broader range of wavelengths without recalibrating the endoscope.

### 1.3. Bandwidth of multimode fibres

The impact of the spatial light modulator on the wavelength tuning range (referred to as the *bandwidth*) was discussed in Section 1.2. Another wavelength-dependent element in the setup which limited the wavelength tuning range was the multimode fibre. The bandwidth of the commercial fibres is typically specified at 850 nm or 1300 nm, wavelengths typically used for telecommunication applications and specified in the units of  $\text{MHz}\cdot\text{km}^{-1}$ . However, it is not immediately apparent how this specified value corresponded to the wavelength tuning range when the multimode fibre was used as an endoscope. In addition, the bandwidth of the fibres would typically be optimised for the telecommunication wavelengths and could be significantly different for wavelengths used for imaging. Consequently, the bandwidth of different multimode fibres was measured using the fibre imaging system.

The bandwidth of the step-index fibres was distinctively lower than any of the graded-index fibres. The impact on the wavelength tuning range is demonstrated in Figure 1.4. The endoscope was calibrated at 780 nm for both fibre types. Afterwards, the wavelength

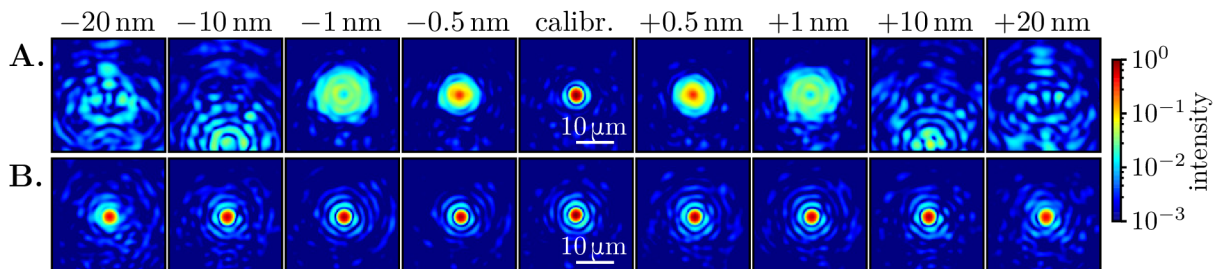


Figure 1.4: Focused points after the wavelength was tuned from the wavelength used for calibration for **A.** a step-index fibre (Thorlabs FG050LGA) and **B.** a graded-index fibre (Thorlabs GIF50E).

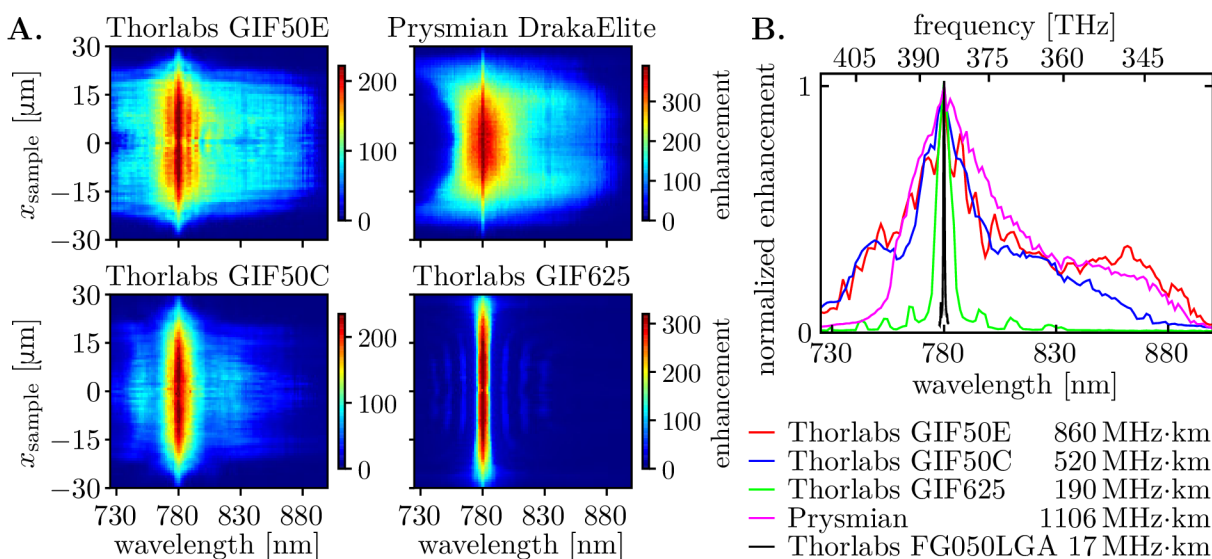


Figure 1.5: Bandwidth measurement for different fibre types. **A.** Enhancement along a line across the field of view after the wavelength was tuned from the calibration wavelength of 780 nm. **B.** Comparison of the bandwidths. The legend shows the measured bandwidths.

of the laser was tuned away from this value while still monitoring the focused point on the camera in the calibration module. While for the graded-index fibre, the focused points persisted over tens of nanometres, for the step-index fibre, it completely vanished within less than one nanometre.

The bandwidth measurement was performed in Figure 1.5, similarly to the measurement in Figure 1.2C,D. The bandwidth of each fibre was calculated as a FWHM of the enhancement averaged across the field of view. The results show a significant difference between the graded-index fibres. The highest bandwidth was measured for the Prysmian fibre, making it optimal for non-linear imaging. Thorlabs GIF50E and Thorlabs GIF50C fibres, despite their relatively high bandwidth, were unsuitable for non-linear imaging due to the low numerical aperture. In addition, by measuring the bandwidth for three different lengths of the fibre, it was verified that the bandwidth was inversely proportional to the length of the fibre.

## 1.4. Femtosecond laser focusing

The bandwidth of multimode fibres affects their ability to focus broadband light, such as light from pulsed lasers. The effect is demonstrated in Figure 1.6, where three different fibres were used to focus light from the femtosecond laser. The Prysmian fibre had a larger bandwidth than the spectral width of the laser and produced a point with a power ratio (and size) comparable to the values achieved with a CW laser. The bandwidth of Thorlabs GIF625 fibre was lower than the spectral width of the laser, which caused a lower power ratio. As discussed in Section 1.3, bandwidth of step-index fibres (here, Thorlabs FG050LGA) was much lower than graded-index fibre. The focused point thus had a meagre power ratio. This shows the importance of choosing a high-bandwidth fibre when using a pulsed source.

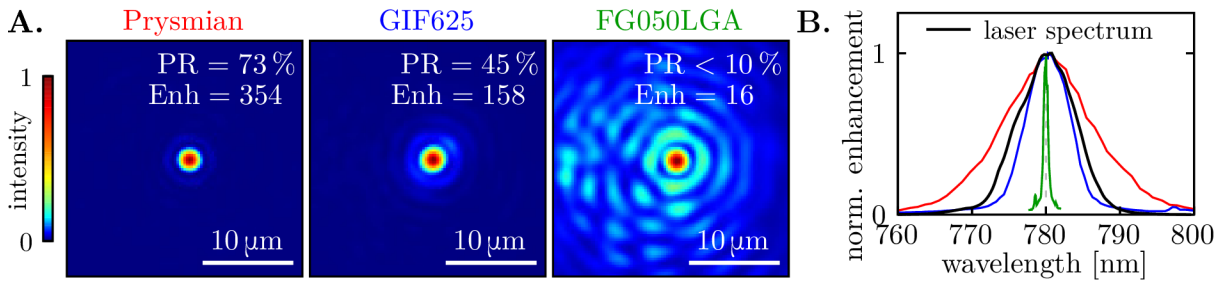


Figure 1.6: Femtosecond laser focusing through a multimode fibre. **A.** Focused points created using the femtosecond laser for two graded-index and one step-index fibres. **B.** Comparison of the bandwidth of the three fibres and the spectrum of the laser.

## 1.5. Spectral phase of the focused point

Controlling the pulse length in the imaging plane is essential for non-linear imaging. When the laser pulse propagates through the multimode fibre, it broadens due to dispersion. Thus, the dispersion must be compensated to obtain a transform-limited pulse in the sample plane.

The spectral phase was measured twice: with and without the fibre, to describe the pulse behaviour after being propagated through the fibre. The difference was the spectral phase change introduced by the fibre. The group delay dispersion introduced by the fibre was calculated using a polynomial fit. This value was then used to calculate the group velocity dispersion (GVD). The spectral phase of the focused point was measured using the tunable CW laser by overlapping the focused point on the camera with the reference beam.

The measured spectral phase for two lengths of the Prysmian fibre, as well as the spectral phase measured with no fibre in the setup are in Figure 1.7A. After subtracting the spectral phase measured without the fibre, the spectral phase introduced by the fibre (i.e., the dispersion of the fibre) was calculated. Figure 1.7b shows the difference for two fibre lengths and five positions of the focused point across the field of view. Performing a polynomial fit of the measured spectral phase yielded the group velocity dispersion value of  $50 \text{ fs}^2 \cdot \text{mm}^{-1}$ . This value was independent of the position of the output point, which implies that a standard pulse compressor, such as a prism compressor, can compensate

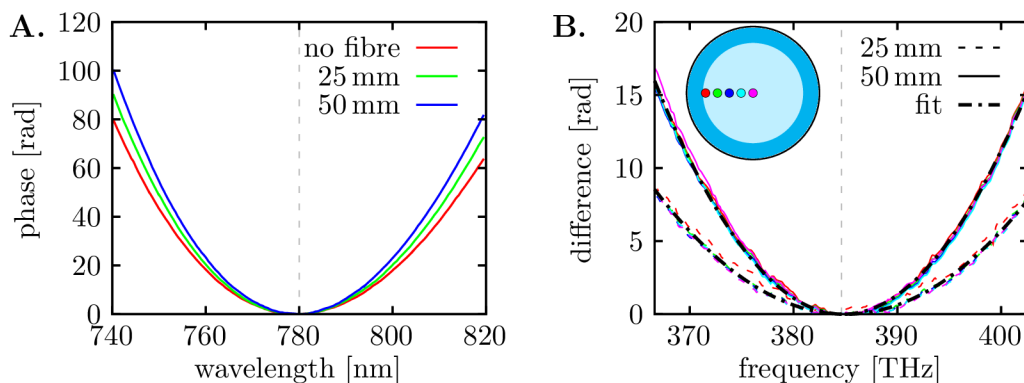


Figure 1.7: **A.** Spectral phase of the focused point measured without a fibre and for two fibre lengths. **B.** Spectral phase difference introduced by the fibre for two fibre lengths and multiple positions of the focused point across the field of view.

for the dispersion introduced by the fibre. In addition, it was found that the spectral phase was purely parabolic, i.e., the fibre introduced no third-order dispersion.

## 1.6. Summary

In this chapter, a multimode fibre endoscope was characterised with the goal to efficiently focus light from a pulsed laser source and allow non-linear imaging through a single multimode fibre.

An experimental setup was built, which combined a tunable continuous-wave laser and a tunable femtosecond laser as a light source. The system included polarisation control of the beam coupled into the fibre, which was crucial for achieving high focus quality using graded-index fibres, which (unlike step-index fibres) do not maintain circular polarisation. Introducing the polarisation control for pulsed lasers necessitated implementing phase drift correction during the imaging (without access to the distal end of the fibre), which made the focused point stable over long periods. The system was then used to characterise the wavelength-dependent behaviour of different multimode fibres.

When tuning the wavelength after the calibration of the fibre, the quality of the focus drops. The degradation was caused by two factors: the wavelength dependence of the optics projecting the pattern on the proximal end of the fibre and on the fibre itself. The most wavelength-dependent component in the system was the spatial light modulator, used in off-axis configuration. The holograms displayed on the SLM have a form of a sum of diffraction gratings. This grating-like behaviour causes the pattern projected on the proximal end to shift with wavelength. Two methods for correcting the wavelength dependence were tested. Since the dispersion of the hologram is known, it can be recalculated for another wavelength (SLM-based correction). Another option is using another wavelength-dependent optical element, such as a prism, to compensate for the dispersion of the SLM (prism-based correction). The SLM-based correction provided a wider wavelength tuning range. Consequently, it was used to measure the bandwidth of different fibres, where the wavelength had to be tuned over a range of many tens of nanometres. On the other hand, the prism-based correction does not require recalculating the holograms while still providing a sufficient level of compensation for many applications, such as targeting different Raman shifts during CARS imaging.

## 1. WAVELENGTH-DEPENDENT BEHAVIOUR OF A FIBRE ENDOSCOPE

After the dispersion of the SLM was compensated for, the bandwidth of different fibres was measured. Different types of fibres were calibrated using a tunable continuous-wave laser, and the quality of the focus was observed after the wavelength of the laser was tuned from the wavelength used for the calibration. Graded-index fibres were able to maintain the focus over a few tens of nanometres (for a 5 cm long piece of fibre). The difference in the bandwidth of different graded-index fibres was, however, almost an order of magnitude, demonstrating that choosing the suitable fibre is crucial for non-linear imaging. The highest bandwidth was measured for the Prysmian DrakaElite fibre.

The bandwidth directly affects the ability of the fibre to focus light from pulsed light sources and, thus, its suitability for non-linear imaging. The suitability for non-linear imaging was demonstrated by calibrating the fibres with a femtosecond laser. With a graded-index fibre with a bandwidth higher than the spectral width of the laser, the power ratio of the focused point was similar to one achieved with a narrow-band continuous-wave laser. Due to using a high-bandwidth fibre and controlling the input polarisation, the achieved power ratios were significantly higher than in previous demonstrations of focusing femtosecond pulses through multimode fibres. Conversely, the low bandwidth of step-index fibres renders them unsuitable for pulsed lasers, as the achievable power ratios are very low, and the resulting point spread functions are much longer than expected from the numerical aperture.

The spectral phase of the focused point was measured to characterise the dispersion of the fibres and examine the options for its compensation. For the Prysmian DrakaElite fibre, the group velocity dispersion was measured to be  $50 \text{ fs}^2 \cdot \text{mm}^{-1}$  at 780 nm, with almost no third order dispersion. This value was independent of the position of the focused point. Thus, a standard pulse compressor, such as a prism pulse compressor, is sufficient to compensate for the group velocity dispersion in the multimode fibre when used for non-linear imaging.

Results presented in this chapter constitute a substantial step towards implementing coherent anti-Stokes scattering imaging and possibly other non-linear imaging techniques through a multimode fibre endoscope and were published in [20].



## 2. Coherent anti-Stokes Raman scattering through fibre

Confocal and multi-photon fluorescence microscopy has become state-of-the-art imaging techniques for imaging living organisms. For many applications, however, labelling the sample is not an option and other imaging techniques with molecular specificity are needed. One such technique is confocal Raman microscopy [25], which allows three-dimensional label-free imaging. Spontaneous Raman imaging, however, requires high excitation powers and very long integration times, mostly incompatible with in-vivo imaging. These shortcomings can be overcome by the use of coherent Raman scattering (CRS) techniques, such as stimulated Raman scattering (SRS) or coherent anti-Stokes Raman scattering (CARS) [18, 26, 27]. Compared to spontaneous Raman microscopy, CARS microscopy offers not only orders of magnitude shorter per-pixel integration times [28], but also has higher biochemical specificity [29]. Typical applications of CARS imaging include optical biopsies for diagnosing tumours and other diseases [19, 30–32], label-free imaging of lipid-rich tissue structures such as myelinated axons [33] or lipid droplets [34].

In CARS, the oscillations of the molecules are driven by the difference frequency between the pump and Stokes beam. When this frequency difference approaches a transition of the dielectric medium, the oscillations are driven very efficiently and can be probed by the probe beam, generating anti-Stokes emission. Since CARS is a coherent process, not only the energy but also the momentum is preserved. Due to the phase-matching condition, the CARS signal is generated predominantly in the forward direction, making epi-detection reliant on scattering [35].

Both linear and non-linear Raman imaging is also used in endoscopy, including biomedical applications [28, 36]. The endoscopes are, however, typically bulky with an outer diameter of a few millimetres. While this might be acceptable for many applications, many others could benefit from the significantly smaller dimensions of multimode fibre endoscopes. In Chapter 1, it was demonstrated that focusing light from pulsed laser sources through a multimode fibre endoscope is possible. These results open up possibilities for implementing non-linear imaging techniques through multimode fibres. This chapter presents the first implementation of coherent anti-Stokes Raman scattering imaging through a single multimode fibre.

### 2.1. Optical setup

The setup for CARS imaging using a picosecond laser system (Figure 2.1) was based on the setup used for fibre characterisation described in Chapter 1. Consequently, only the differences are described here.

## 2. COHERENT ANTI-STOKES RAMAN SCATTERING THROUGH FIBRE

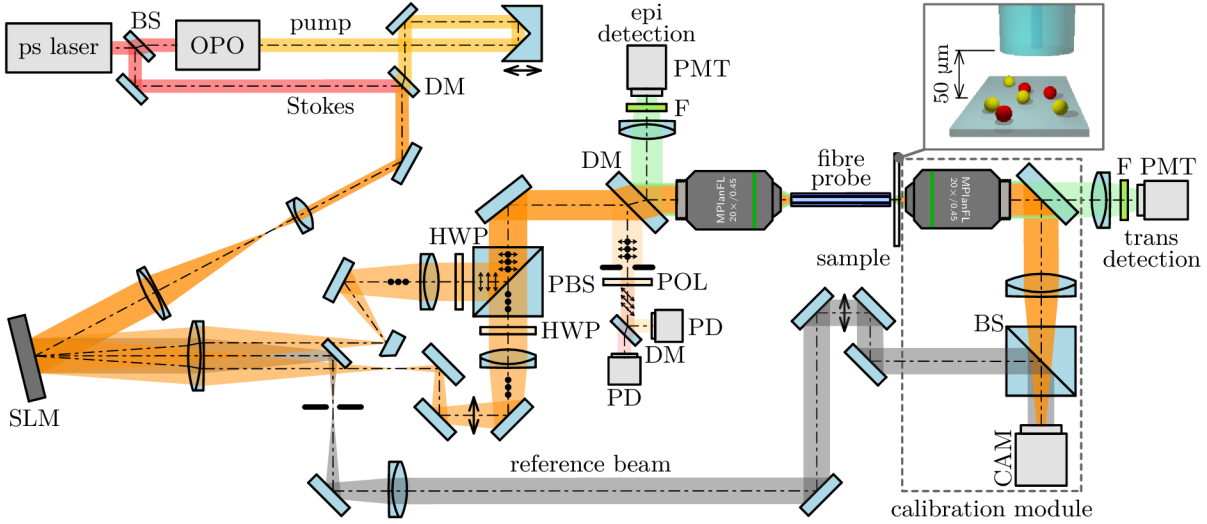


Figure 2.1: Simplified drawing of the setup for CARS imaging through a multimode fibre using a picosecond laser system. BS – non-polarising beamsplitter CAM – camera, DM – dichroic mirror, F – filter, HWP – half-wave plate, SLM – spatial light modulator, PD – photodiode, PMT – photomultiplier tube, PSB – polarising beamsplitter cube.

The light source consisted of a 832 nm picosecond laser (Coherent Mira HP-P, used as a CARS Stokes beam) and an optical parametric oscillator (OPO; APE OPO, used as a CARS pump beam). Both beams were combined on a dichroic mirror with an adjustable time delay of the pump beam. Focusing of the two wavelengths simultaneously necessitated using two photodiodes to stabilise the two input polarisation optical paths, one for each beam. For simplicity, no SLM dispersion compensation was used. Prysmian DarkaElite graded-index fibre was used for the experiments. The probe length was 30 mm to 35 mm.

For imaging in transmission, the signal was collected through the objective in the calibration module, filtered using a short-pass filter and a band-pass filter and focused onto photomultiplier tube (PMT). For epi-detection, the signal collected through the fibre was reflected off a long-pass dichroic mirror, filtered using a short-pass filter and a band-pass filter and focused onto a PMT. The signal from the PMT was averaged during the entire integration time (typically 2 ms).

### 2.2. Imaging of polymer beads

CARS imaging through multimode fibre was tested on 2  $\mu\text{m}$  polystyrene (PS) and 2.5  $\mu\text{m}$  polymethyl methacrylate (PMMA) beads on a cover glass. In Figure 2.2, a single layer of PS beads on a cover glass was imaged in transmission and with epi-detection. As expected, the signal in epi was significantly weaker, and the image was thus noisy. Nevertheless, the beads were visible. Despite the low collection efficiency, this experiment demonstrated that epi detection through the multimode fibre was possible.

The chemical sensitivity of CARS is demonstrated in Figure 2.3. Two samples were imaged with the signal being detected in transmission. The wavelength of the OPO was tuned, which resulted in different Raman shifts being excited. Figure 2.3C shows the measured spectra of PS and PMMA, corrected for the limited wavelength tuning range of the system and the variations of the OPO power. The bandwidth of the system

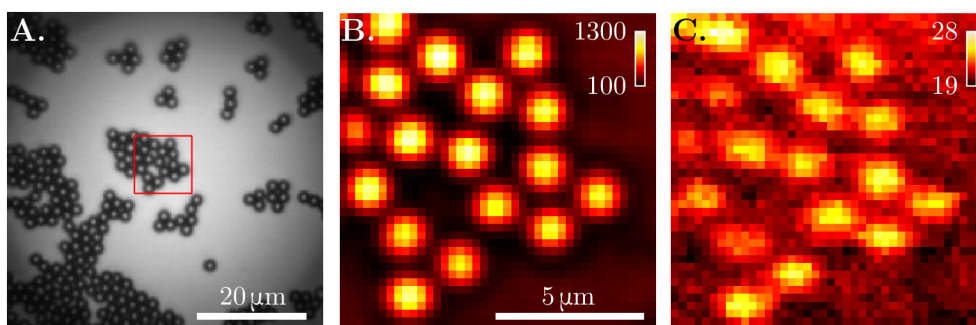


Figure 2.2: **A.** Brightfield image of the sample ( $2\mu\text{m}$  polystyrene beads on a glass slide). **B.** CARS image of the highlighted area with the signal collected in transmission. **C.** CARS image with epi-detection.

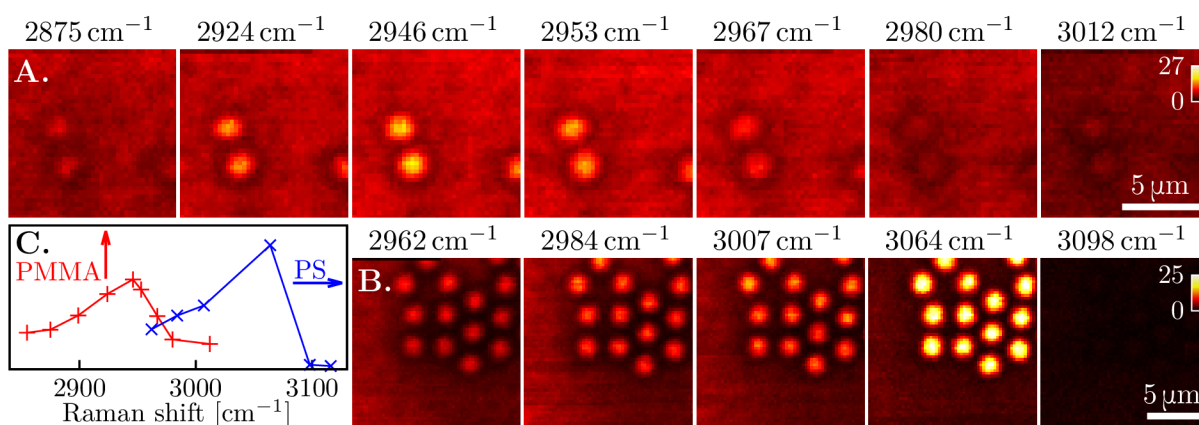


Figure 2.3: Wavelength sweep of  $2\mu\text{m}$  PS and  $2.5\mu\text{m}$  PMMA beads on a cover glass. **A.**, **B.** CARS images of beads taken at different Raman shifts. **C.** Intensity of the beads as a function of the Raman shift. The lines are a guide to the eye.

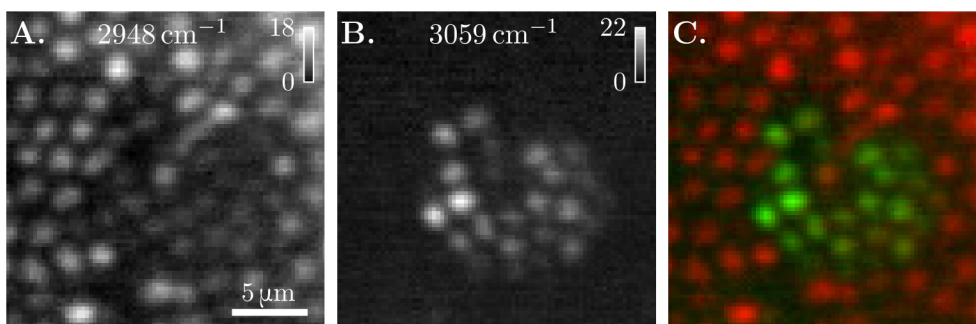


Figure 2.4: Chemical contrast on CARS imaging of a mix of PS and PMMA beads with epi-detection. **A.**, **B.** CARS images captured at two different pump wavelengths (corresponding to the Raman shifts in the captions). **C.** Overlay of both images.

## 2. COHERENT ANTI-STOKES RAMAN SCATTERING THROUGH FIBRE

was sufficient to cover both the PS and PMMA resonances using a single calibration at  $2958\text{ cm}^{-1}$ .

Figure 2.4A,B shows a CARS images of a thicker layer of a mix of PS and PMMA beads, captured at two different Raman shifts (corresponding to the peaks in Figure 2.3C). The thicker layer of beads was used to increase scattering in the sample and, thus, the intensity of the epi-collected signal. Such scattering samples better mimicked imaging inside a tissue. Figure 2.4C shows an overlay of both images, demonstrating the chemical contrast allowing the differentiation between PS and PMMA.

### 2.3. Summary

In this chapter, the first implementation of coherent anti-Stokes Raman scattering (CARS) imaging through a multimode fibre was presented.

An endoscopic system developed and characterised in Chapter 1 was used with a picosecond laser system consisting of a picosecond laser (Stokes beam) and an optical parametric oscillator (pump beam). Both spatially overlapping beams were focused through a multimode into the same point, allowing the generation of the CARS signal in the sample.

CARS imaging of  $2\text{ }\mu\text{m}$  polystyrene (PS) and  $2.5\text{ }\mu\text{m}$  polymethyl methacrylate (PMMA) beads on a glass slide was demonstrated. The signal generated in the sample was collected in transmission as well as through the same fibre used for the delivery of the excitation beam, i.e., epi-detection. The epi-detection was possible despite the CARS signal being generated predominantly in the forward direction and thus relying on scattering (for thick layers of beads) or the reflection on the air to glass interface (for a single layer of beads). These results show that the fibre endoscope could be used for endoscopic applications inside the tissue. This potentially paves the way for the implementation of other imaging techniques with similar emission patterns like stimulated Raman spectroscopy (SRS) or third-harmonic generation (THG), where epi-detection is also reliant on back-scattering from the tissue.

Imaging with chemical contrast was demonstrated on a mix of PS and PMMA beads. Changing the wavelength of the pump beam allowed different Raman shifts to be targeted. Combining the two images could determine the composition of the mixed sample.

The demonstrated CARS implementation was, unfortunately, slow compared to other endoscopic CARS implementations, where a single image typically takes a few seconds at maximum, compared to several minutes (depending on the size of the field of view and resolution) demonstrated here. The limiting factor in speed was the refresh frequency of the liquid crystal spatial light modulator, set to about  $55\text{ Hz}$  (pixels per second). A more efficient implementation of the timing, could increase the speed to  $170\text{ Hz}$  for the same integration time. Nonetheless, a liquid crystal SLM would still be slower compared to digital micromirror devices (DMDs) used for linear imaging through multimode fibres, typically operating at a refresh frequency of about  $23\text{ kHz}$ . Currently available DMDs are binary amplitude modulators, thus inherently inefficient. Additionally, they suffer from significantly higher dispersion than SLMs, due to using tilted micromirrors, which would have to be compensated for. These attributes make them hard to use for non-linear imaging, where high excitation powers and pulsed laser sources are required. In future, however, phase-modulating micromirror devices (PLMs) could provide efficiency approaching one of the liquid-crystal SLMs, while maintaining fast refresh rates.

The diameter of the fibre probe (Prysmian DrakaElite, about 30 mm long) was  $125\ \mu\text{m}$  with a  $50\ \mu\text{m}$  diameter field of view (FoV) and numerical aperture of 0.3. The dimensions of the probes were thus significantly smaller compared to other endoscopic CARS approaches, where the probes typically have a diameter of a few millimetres. For instance, in [37], the diameter of the probe was 2.2 mm (with a  $230\ \mu\text{m}$  field of view), in [38] it was 2.4 mm ( $180\ \mu\text{m}$  FoV), and in [39] 8 mm (about  $500\ \mu\text{m}$  FoV). The small dimensions make the multimode fibre probes significantly less invasive than any other CARS endoscope reported.

The endoscope presented here, however, did not have a similar spatial resolution to the other discussed endoscopes due to the relatively low numerical aperture of the fibre used. Nevertheless, the numerical aperture is not unreasonably small, as shown in [40]. The resolution of a multimode fibre endoscope depends only on the numerical aperture of the fibre and is thus independent of the fibre diameter. Consequently, if higher numerical aperture graded-index fibres become available in the future (providing that such fibres have sufficient bandwidth), the resolution could be increased without increasing the endoscope size. Thus the amount of damage this endoscope would have for imaging inside the tissue.

To conclude, this study demonstrates that it is feasible to perform label-free CARS imaging with chemical contrast through a single multimode fibre of structures as small as  $2\ \mu\text{m}$  with epi-detection. The results presented in this chapter were published in [21], which is the first demonstration of label-free non-linear imaging with chemical contrast through a multimode fibre endoscope.

## 2. COHERENT ANTI-STOKES RAMAN SCATTERING THROUGH FIBRE

# 3. Non-linear imaging using a femtosecond laser

In Chapter 2, coherent anti-Stokes Raman scattering (CARS) imaging through a single multimode fibre with a chemical contrast was demonstrated. The chemical contrast was achieved by using a narrowband picosecond laser system and tuning the wavelength of one of the two excitation beams, which resulted in different molecules being excited. CARS imaging can also be performed using femtosecond lasers, which are more commonly available in bio-imaging labs and more suitable for other imaging modalities like two-photon excitation fluorescence (TPEF) or second-harmonic generation (SHG) imaging. When such a broadband laser source is used, the spectral resolution is reduced due to the large instantaneous bandwidth of the source. To get a sufficient spectral resolution with a broadband laser source, spectral focusing is commonly implemented [41]. In essence, both the pump and the Stokes beams are stretched to decrease the instantaneous bandwidth of the source.

In this chapter, an implementation of coherent anti-Stokes Raman scattering (CARS) and two-photon excitation fluorescence (TPEF) through a single multimode fibre and using a femtosecond laser as the excitation source is presented. In addition, the endoscopic system shown here can perform polarisation-resolved second-harmonic generation (SHG) imaging. The main focus of this chapter is the suppression of a strong background signal during CARS imaging, which is generated in the fibre probe due to the self-imaging property of graded-index fibres. A composite probe, which significantly reduces the background, is proposed and characterised in terms of its focusing performance and dispersion. The probe is then used to demonstrate multimodal CARS and TPEF imaging of fixed mouse tissue.

## 3.1. Optical setup

A simplified drawing of the setup for non-linear imaging through a multimode fibre using a femtosecond laser is shown in Figure 3.1. The setup was based on the system presented in Chapter 2 with implementing some features introduced in Chapter 1. Only the differences between the systems are discussed here.

The femtosecond laser (Coherent Chameleon Discovery) was the excitation source. Both outputs of the laser were used. The fixed beam at 1040 nm was used as CARS Stokes beam could also be used as the excitation beam for SHG imaging. The tunable beam was used as CARS pump beam and the excitation beam for TPEF imaging.

For CARS imaging, glass blocks made of SF57 glass were added to both beams to stretch the pulses and implement spectral focusing. Two 110 mm long blocks were inserted in both beams. Including the dispersion introduced by the rest of the setup, the fibre and

### 3. NON-LINEAR IMAGING USING A FEMTOSECOND LASER

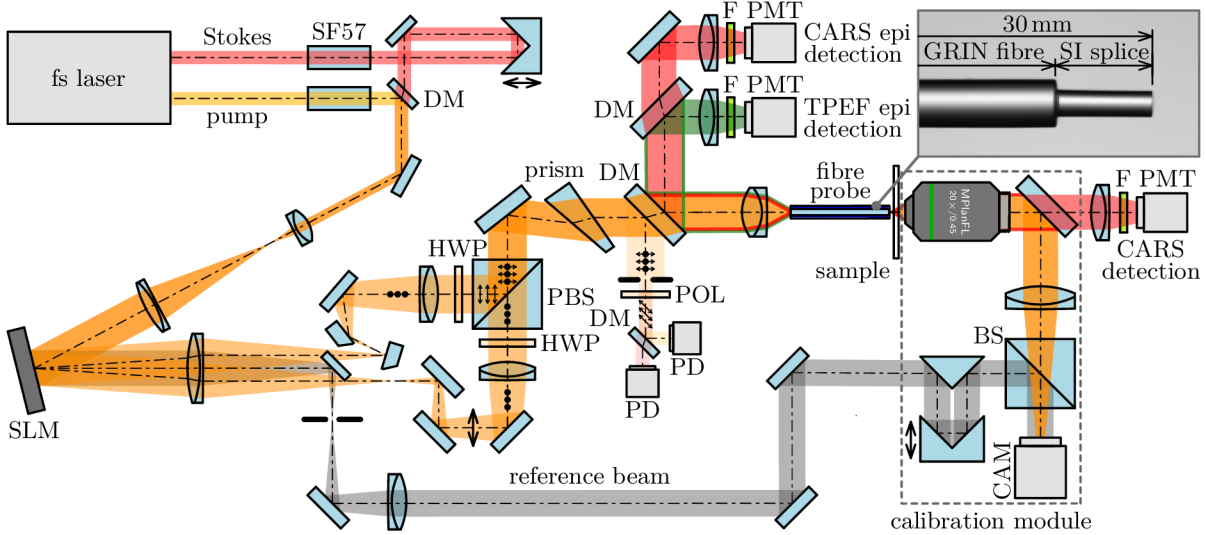


Figure 3.1: Simplified drawing of the setup for non-linear imaging through a multimode fibre using a femtosecond laser. BS – non-polarising beamsplitter, CAM – camera, DM – dichroic mirror, F – filter, HWP – half-wave plate, SLM – spatial light modulator, PD – photodiode, PMT – photomultiplier tube, POL – polariser, PSB – polarising beamsplitter cube, SF57 – glass blocks. The inset shows the composite probe for CARS background suppression.

the pre-compensator built-in the tunable output of the laser, both beams were equally stretched by  $46500 \text{ fs}^2$  of GDD. The pulse lengths in the sample plane thus were about 1300 fs and 930 fs for the pump and Stokes beams, respectively.

A wedge prism was used to compensate for the dispersion of the SLM, as discussed in Section 1.2. Unlike in the previous setups, the fibre was mounted vertically, which was more suitable for tissue imaging, as the tissue is typically submerged in a liquid. The signals could be detected both in transmission (mostly used for testing) and in epi (for tissue imaging) on three PMTs in total. In epi, two channels were available. The green channel was used for TPEF and SHG imaging and the red one for CARS.

### 3.2. Background suppression

When fibres are used for delivery of the excitation beams for coherent anti-Stokes Raman scattering imaging, an unwanted background signal can be generated inside the fibre itself due to four-wave mixing (FWM) and other non-linear processes [39, 42]. This signal is of the same wavelength as the CARS signal (which is also a FWM process) generated in the sample. Consequently, removing it using spectral filters is impossible when the same fibre delivers the excitation beams and collects the CARS signal. Due to the self-imaging property of graded-index fibres, the focused point created in the sample plane close to the distal end of the fibre was re-imaged multiple times inside the fibre itself. The self-imaging distance ( $\approx 400 \mu\text{m}$ , depending on the type of the fibre) was similar at both the pump and the Stokes wavelengths, making the points for the pump and the Stokes beams overlap inside the fibre in space. In addition, the self-imaging distance was short enough so that the points for the pump and Stokes beams overlapped time, at least for a few points closest to the distal end of the fibre. In these points, a potentially strong signal was generated by four-wave mixing.



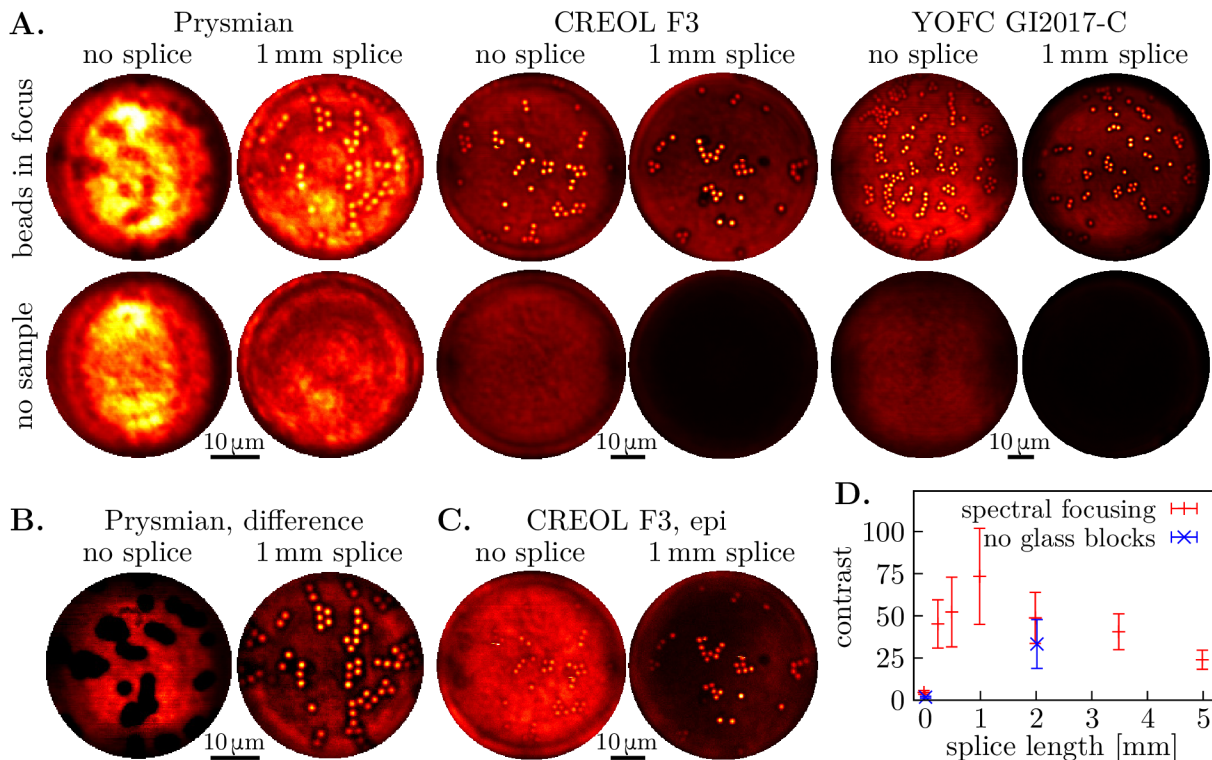


Figure 3.2: Background generated in the fibre and its suppression by using the spliced probe. **A.** Images of  $2\mu\text{m}$  PS beads and images with no sample in focus captured using different probes. **B.** Simple subtraction of the background does not yield a correct image. **C.** Images with epi-detection. **D.** Contrast of the beads for different splice lengths.

The impact of the background generated in the fibre on CARS imaging is demonstrated in Figure 3.2. Here,  $2\mu\text{m}$  PS beads on a glass slide were imaged using different fibre probes. Afterwards, the sample was removed, and another image was captured to evaluate the intensity of the unwanted background. Ideally, no signal should be generated when no sample is in focus. The measured images, however, showed a strong signal. For the Prysmian fibre, the signal generated in the fibre was, in fact, of a higher intensity than the signal generated in the beads. The background intensity for the CREOL and YOFC fibre was comparable to the non-resonant signal generated in the glass slide.

The background was generated due to the high-intensity points created due to the self-imaging property of the graded-index fibres. Using a fibre which did not have a self-imaging property would not allow the creation of high-intensity points. Instead, the beam would be spread into random speckles, with intensity supposedly low enough not to generate a noticeable signal. Step-index fibres do not support self-imaging. However, the bandwidth of step-index fibres is very low. Instead, the distal end of the fibre had to be modified not to allow the creation of high-intensity points inside the fibre. Any modification that would break the focused points into random speckles would decrease the intensity of the background. Here, a short piece of a step-index fibre (CeramOptec Optran Ultra WFGE, tapered to have the same core diameter as the graded-index fibre) was spliced to the distal end of the graded-index fibre, forming a composite probe (see inset in Figure 3.1).

Figure 3.2D shows the impact of the splice length (for the CREOL F3 fibre) on imaging polystyrene beads. The total length (the graded-index part plus the step-index splice) of all probes was 30 mm. For each splice length, a signal-to-background ratio was evaluated.

### 3. NON-LINEAR IMAGING USING A FEMTOSECOND LASER

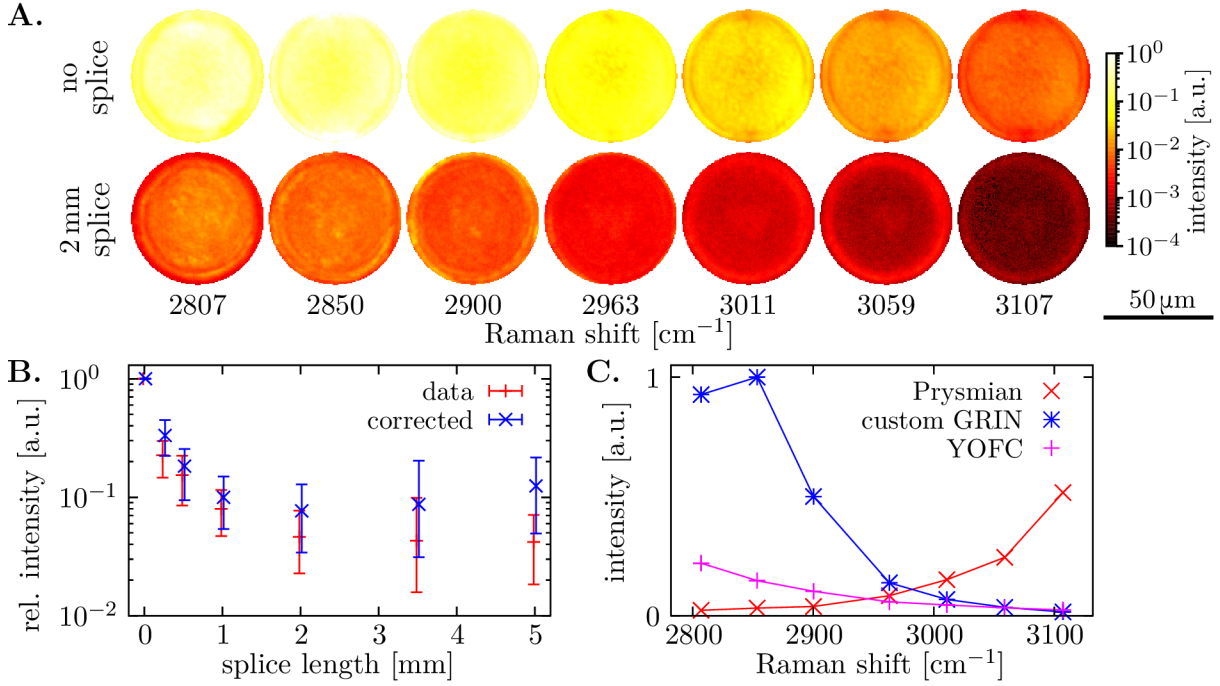


Figure 3.3: Characterisation of the background generated in the fibre. **A.** Images taken with no sample in the system. **B.** Suppression of the background signal. **C.** Wavelength dependence of the background signal.

This ratio increased with increasing splice length up to a 1 mm long splice. Afterwards, the ratio started to drop again. This drop suggests that while the intensity of the background decreased with the increasing length of the splice, the intensity of the CARS signal excited in the sample dropped. For polystyrene, the optimal length of the splice was about 1 mm.

The spectral dependence of the background fibre was tested by imaging at different Raman shifts (covering Raman shifts typically used for bio-imaging of lipids, proteins and DNA [43] and PS and PMMA) with no sample in the system. The images (with the signal being collected in transmission) captured during this experiment are in Figure 3.3. This figure shows both the spectral dependence of the signal and the suppression of the background. Figure 3.3B shows that increasing the length of the splice decreased the intensity of the background signal. The actual level of suppression depended on the Raman shift, but for splices 2 mm or longer, the suppression was at least an order of magnitude. Correcting the data for the drop of power ratio and increase of spot size measured in Figure 3.4 showed an optimal length of the splice of 2 mm. For this splice length, the signal-to-background ratio should be maximal. By CARS imaging of polystyrene beads in Figure 3.2, the optimal length was determined to be 1 mm. The spectral dependence of the background likely caused the difference. Nevertheless, a 1 mm to 2 mm long splice provided a level of background suppression sufficient for imaging.

### 3.3. Focusing performance of composite probes

The focusing performance of the spliced probes was evaluated by measuring the three-dimensional point spread functions (Figure 3.4A). For the step-index fibre, the point spread function was significantly longer (despite the fibre having a higher numerical aperture) and the intensity of the background was much higher (i.e., the power ratio was

### 3.3. FOCUSING PERFORMANCE OF COMPOSITE PROBES

lower). These effects were both caused by the low bandwidth of the fibre and were expected of a step-index fibre. The point spread functions for the spliced probes were, in general, more similar to the graded-index fibre, as the length of the step-index splice was too short to noticeably impact the focusing performance of the probe.

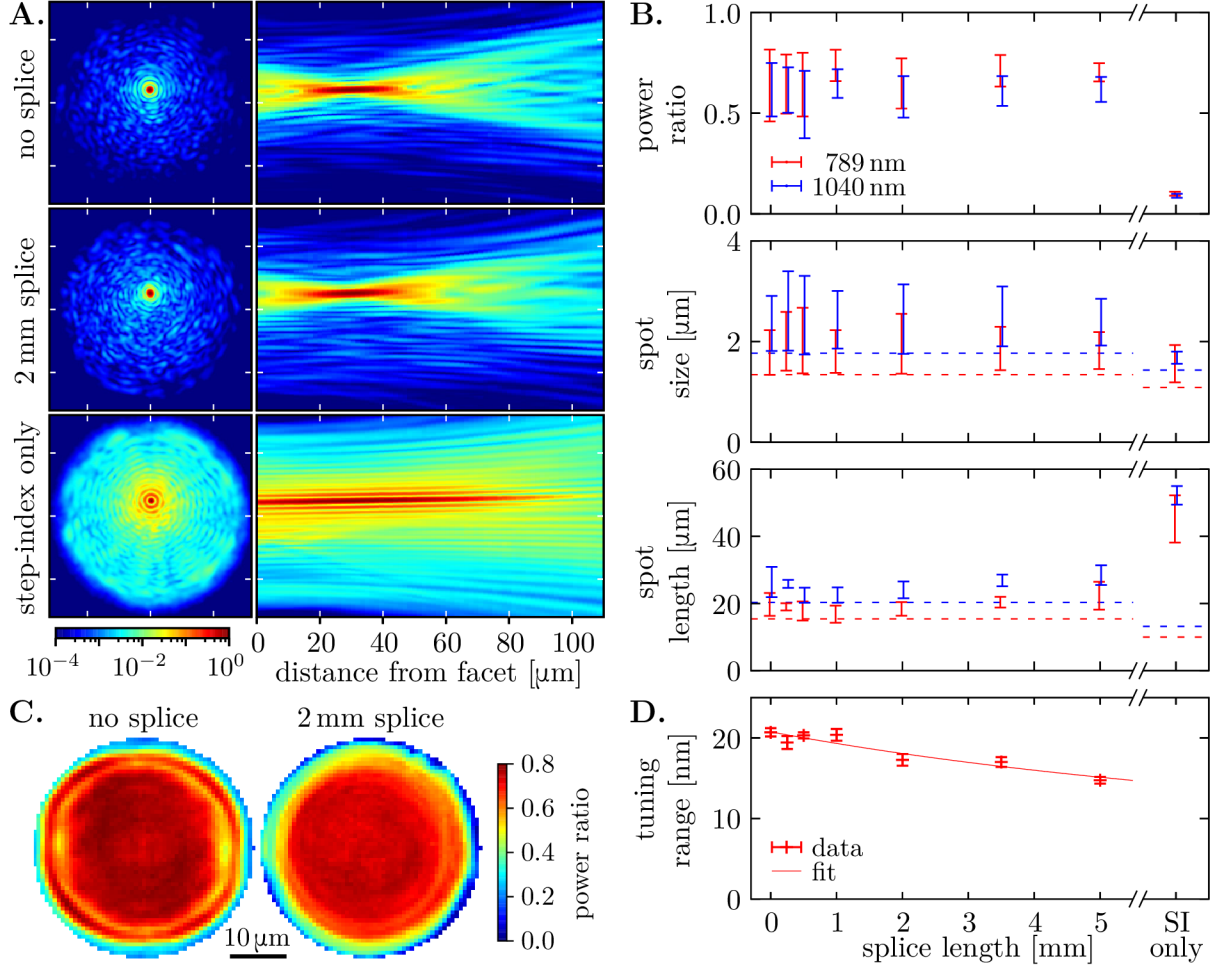


Figure 3.4: Focusing performance of the spliced probes. **A.** Measured point spread functions. **B.** Power ratio, spot size and spot length at two wavelengths as a function of the splice length (the total length the probe was 30 mm). The bars show the range of values across the field of view. The dashed lines are diffraction-limited values. **C.** Power ratio for different points across the field of view. **D.** Wavelength tuning range at 789 nm measured using the femtosecond laser.

Figure 3.4B shows the power ratio and lateral and axial spot size as a function of the splice length. The error bars show the range of the values across the field of view. The error bar length thus indicates the difference between the maximal and minimal value in the field of view. Typically, the minimal spot size and highest power ratio were achieved for points close to the axis and the maximal spot size and lowest power ratio at the edge of the field of view. For the graded-index fibre and fibres with a splice length up to 2 mm, both the lateral and axial spot sizes approached the diffraction-limited values for the numerical aperture of the fibre. For longer splices, the size of the points increased, and the maximal power ratio decreased. Figure 3.4C shows the power ratio across the field of view. The data confirms that the maximal achievable power ratio decreased for

### 3. NON-LINEAR IMAGING USING A FEMTOSECOND LASER

the spliced fibre, nevertheless, it was more homogeneous across the field of view. In this regard, the probes with long splices behaved more like step-index fibres.

The bandwidth of step-index fibres is significantly lower than graded-index fibres, and they suffer from the chromato-axial memory effect [44]. The step-index splice thus decreased the total bandwidth of the spliced probes compared to the bandwidth of the pure graded-index fibre. Figure 3.4D shows that the wavelength tuning range indeed decreased with the increasing length of the splice. However, for the splice lengths used here, the change was small and thus had only a minor impact on imaging.

The chromato-axial memory effect in step-index fibres results in the focused point moving with wavelength along the axis of the fibre. The three-dimensional point spread functions were measured using a tunable CW laser after the wavelength was tuned from the value used for the calibration to quantify the shift for the spliced fibres. For the CeramOptec step-index fibre tapered to 70  $\mu\text{m}$  outer diameter (and the numerical aperture of the beam limited to 0.30), the axial shift was  $-0.33 \mu\text{m}\cdot\text{nm}^{-1}\cdot\text{mm}^{-1}$  (negative, as the point shifted closer to the fibre for longer wavelengths). For the CREOL F3 graded-index fibre, the shift was  $-0.007 \mu\text{m}\cdot\text{nm}^{-1}\cdot\text{mm}^{-1}$ , almost two orders of magnitude lower than shift for the step-index fibre. The shift for the spliced fibres was approximately equal to the total shift caused by the graded and step-index parts. For example, for the probe with 2 mm long splice (that is 2 mm long step-index fibre and 28 mm long graded-index fibre), the shift was approximately four times higher than the shift of the pure graded-index fibre, though still more than an order of magnitude lower than the shift for the pure step-index fibre. Consequently, the shift for the spliced fibre was still small, thus, had a minimal impact on imaging.

## 3.4. Imaging

The imaging capability of the fibre imaging system developed in this thesis was tested on two-photon excitation fluorescence and coherent anti-Stokes Raman scattering imaging of PS and PMMA beads and fixed mouse tissue. Brains and sciatic nerves were obtained from wild-type and transgenic Tg(Thy1-EGFP)MJrs/J transcardially perfused adult mice.

The chemical contrast of CARS was achieved in terms of spectral focusing. Different Raman shifts (within the spectral width of the laser) could thus be excited by changing the time delay between the pump and Stokes beams. The spectral focusing is demonstrated in Figure 3.5 by CARS imaging a mix of 2  $\mu\text{m}$  PS and 2.5  $\mu\text{m}$  PMMA beads on a glass slide. By capturing two images with two different time delays, the two types of beads could be differentiated. Hence, a chemical contrast was achieved using spectral focusing. The result is similar to what was achieved in Figure 2.4 by using a picosecond laser system and tuning the wavelength of the pump beam.

Label-free coherent anti-stokes Raman scattering imaging was demonstrated by imaging a sciatic nerve extracted from a wild-type mouse (Figure 3.6A). The composite fibre probe was used, which consisted of the CREOL F3 graded-index fibre and a 2 mm long step-index splice. The probe was calibrated 30  $\mu\text{m}$  from the facet at 802 nm (pump) and 1040 nm (Stokes), corresponding to Raman shift of 2853  $\text{cm}^{-1}$  (optimal for exciting lipids). The figure shows that the myelin sheaths surrounding the axons were visible as rings in the transversal cut. The images showed no excessive background, confirming that the composite probe suppressed the signal generation in the fibre. An attempt was made to image the same sample using a pure CREOL F3 graded-index fibre (with no splice).

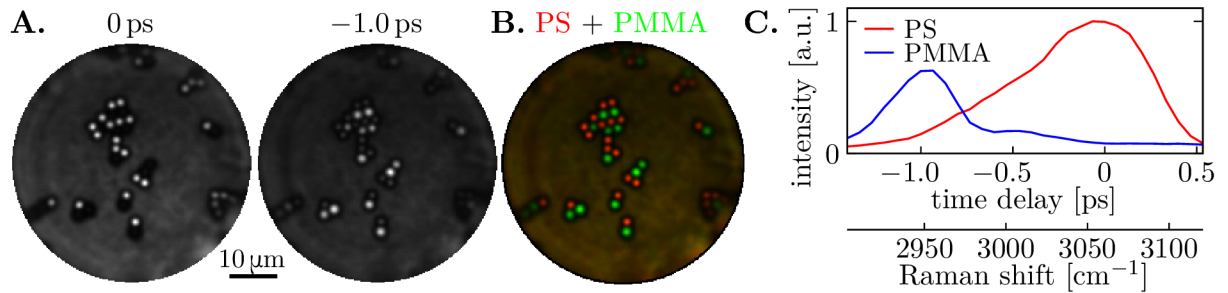


Figure 3.5: Chemical contrast of CARS imaging with spectral focusing. **A.** CARS images of a mix of PS and PMMA beads captured for two different time delays between the excitation beams. **B.** Overlay of both images **C.** Intensity of the beads as a function of the time delay (and corresponding Raman shifts).

However, the intensity of the background was so high that it was impossible to find any structures in the images. The image of the sciatic nerve was taken on the surface of the samples, as the fixed sciatic nerve was too hard to insert the fibre. To demonstrate imaging deep in tissue, myelinated nerve fibres in the corpus callosum were imaged in Figure 3.6B. Here, the fibre was inserted about 1.5 mm deep into the tissue, significantly deeper than could be imaged in a standard scanning microscope.

A whole brain from the transgenic mouse was used to demonstrate two-photon excitation fluorescence imaging (Figure 3.6C). The image show that the endoscope could perform TPEF imaging inside tissue with sufficient signal-to-noise ratio and image somas and surrounding processes.

Multimodal CARS and TPEF imaging is demonstrated in Figure 3.6D. In this image, a surface of a cut from the transgenic mouse brain cerebellum was imaged. The green TPEF channel shows the axons and the red CARS channel shows the myelin sheath.

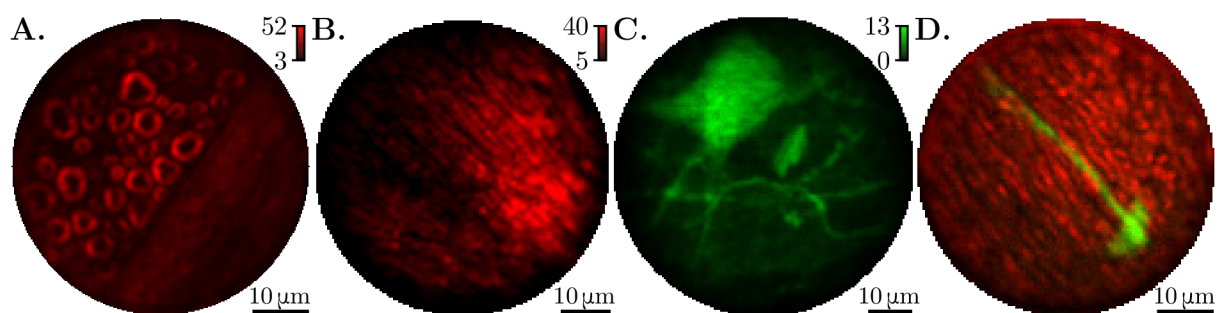


Figure 3.6: CARS and TPEF images of fixed mouse tissue. **A.** CARS image (at  $2853\text{ cm}^{-1}$ ) of a transverse section of a sciatic nerve taken from a wild-type mouse. **B.** CARS image of myelin sheaths in the corpus callosum of a wild-type mouse brain taken with the probe inserted 1.5 mm inside the tissue. **C.** TPEF imaging inside a fixed transgenic mouse brain showing a soma and surrounding processes. **D.** Multimodal CARS (red channel) and TPEF (green channel) imaging on the surface of a fixed cerebellum slice extracted out of a transgenic mouse brain.

### 3.5. Summary

In this chapter, two-photon excitation fluorescence (TPEF) and coherent anti-Stokes Raman scattering (CARS) imaging through a single multimode fibre endoscope using a femtosecond laser was presented.

The system used in Chapter 2 was used and modified to utilise a femtosecond laser with two synchronised outputs (one of them with a tunable wavelength) as an excitation source. In addition, the prism-based SLM dispersion correction was implemented and the pixel rate was increased to about 170 Hz.

After testing CARS imaging of polymer beads using the femtosecond laser, it was realised that a strong background was generated in the fibre probe. This signal, generated via four-wave mixing (FWM), arose from the self-imaging property of graded-index fibres. In essence, the focused points were created not only in the sample plane but also inside the fibre generating a strong background signal, spectrally overlapping with the CARS signal.

In Chapter 2, CARS imaging of PS and PMMA beads was performed using a picosecond laser system. The Prysmian fibre was used, and no noticeable unwanted background signal was observed. When the same fibre was used with the femtosecond laser to probe the same Raman shift, a very strong signal was generated in the fibre. In fact, at this Raman shift and using this fibre, the intensity of the background generated in the fibre was so strong that its suppression by more than an order of magnitude was insufficient to image the polystyrene beads. The reason for this immense difference, unfortunately, remained unexplained. When the strong background in the Prysmian fibre was discovered, performing additional characterisations using the same or a different picosecond laser system was no longer practicable. Since only one of the femtosecond laser outputs was tunable, measuring using different wavelengths (and the same Raman shifts) was impossible. Thus, it was impossible to determine if the background was caused by using femtosecond pulses (despite the pulses being stretched to about one picosecond for spectral focusing), an unfortunate choice of wavelengths or whether there were other causes.

Since the primary cause of the background was not known, the sources of the background had to be suppressed. The field inside the fibre had to be broken into a low-intensity random speckle pattern and uncorrelated for the two wavelengths used for CARS. Completely replacing the graded-index fibre with a step-index fibre (which does not have the self-imaging property and would thus not create the foci) was not feasible due to the low bandwidth. Consequently, a short piece ( $\leq 5$  mm) of a step-index fibre was used and fusion-spliced at the distal end of the graded-index fibre. Thus, the resulting composite probe behaved more like a graded-index fibre and had a relatively high bandwidth while not generating the high-intensity points inside the fibre.

The composite probes allowed imaging of polymer beads on a glass slide. Adding even a 0.25 mm long splice reduced the background. The total reduction was one to two orders of magnitude, depending on the splice length and the Raman shift used. The intensity of the background dropped significantly with the increasing length of the splice. At the same time, however, the intensity of the signal generated in the sample decreased as well. The optimal length of the splice was found to be about 1 mm to 2 mm.

Tissue imaging using the composite probes was performed to test the background suppression on a more realistic sample. The probes were used to image myelinated nerve fibres in a sciatic nerve extracted from a mouse and in the cerebellum of a mouse brain.

The images had sufficient contrast without any noticeable background. When trying to image with a graded-index fibre without the splice, the intensity of the background signal generated in the fibre was so high that no structures were visible. These images showed that adding the short splice to the distal end of the graded-index fibre effectively suppressed the background and made label-free CARS imaging of biologically relevant structures possible. The epi-detection was possible despite the CARS signal being generated predominantly in the forward direction (thus epi-detection relying on scattering in the underlying tissue) and the small collection area of the fibre probe.

In addition to CARS, TPEF imaging of neurons in a fixed transgenic mouse brain was shown. The two non-linear imaging techniques were combined to perform multimodal imaging in the fixed cerebellum.

The presented work thus showed that multimodal imaging through a multimode fibre of structures deep is possible with a sufficient signal-to-background ratio by performing simultaneous CARS imaging of myelin in the white matter, and TPEF imaging of mossy fibres expressing GFP in the cerebellum of a fixed brain from a mouse. The suppression of the background generated in the fibre, the characterisation of the composite probes and the multimodal CARS and TPEF imaging presented in this chapter were published in [22]. Furthermore, the fibre imaging system built for this work was used for the implementation of polarisation-resolved second-harmonic generation imaging through a multimode fibre (not part of this thesis), published in [45]. The fibre polishing system presented here was used for the preparation of the side-view probes in [46], which were used for in-vivo linear fluorescence imaging in mouse brain published in [14].

3. NON-LINEAR IMAGING USING A FEMTOSECOND LASER



# Conclusions

The presented thesis deals with non-linear imaging through a multimode fibre endoscope. The thesis was focused mainly on the technical aspects of implementing non-linear imaging using multimode fibres. The goal was to implement two-photon excitation fluorescence (TPEF) and coherent anti-Stokes scattering (CARS) imaging through a single multimode fibre endoscope.

The first chapter investigated the bandwidth of a multimode fibre imaging system and its impact on focusing a femtosecond laser beam through the multimode fibre. It was found that compensating the dispersion of the off-axis holograms displayed on the spatial light modulator was necessary to use the entire bandwidth of the fibres. As expected, a bandwidth of reasonably long (at least 30 mm) step-index fibre was found too low for using it with a femtosecond laser, making graded-index fibres the type of choice. Nevertheless, a significant difference between the different graded-index fibres tested further emphasised the need for proper selection of the fibre for non-linear imaging applications. This study, partially published in [20], was a substantial step towards efficiently focusing laser pulses through a multimode fibre. Moreover, it enabled implementing non-linear imaging techniques through a single multimode fibre, mainly CARS imaging.

CARS microscopy through a single multimode fibre was demonstrated in the second chapter. CARS imaging of polystyrene and polymethyl methacrylate beads on a glass slide was performed using a picosecond laser and the fibre imaging system developed in the previous chapter. This demonstration, published in [21], has the potential to be the least invasive and fastest label-free endoscopic bio-imaging method with chemical contrast reported so far. It demonstrates that it is feasible to perform CARS imaging through a multimode fibre of structures as small as  $2\ \mu\text{m}$  with integration times as low as 1 ms. Despite the low collection efficiency of the probe, epi-detection was successfully demonstrated, which paves the way for other non-linear imaging techniques such as stimulated Raman spectroscopy (SRS) or third-harmonic generation (THG), where the epi-detection relies mainly on scattering.

The third chapter presented multimodal CARS and TPEF imaging through a multimode fibre. When implementing CARS imaging and using a femtosecond excitation source, a strong background signal generated in the graded-index fibre probe was discovered, which diminished the contrast of the images. This signal was a direct consequence of the self-imaging property of the graded-index fibre, which resulted in high-intensity points inside the probe. A composite probe consisting of a long graded-index fibre and a few millimetres long step-index fibre spliced at the distal end of the probe was proposed to mitigate the issue. This probe, published in [22] and patented, reduced the background by more than an order of magnitude while maintaining sufficient bandwidth for focusing femtosecond pulses, an essential step for CARS imaging of tissue.

## CONCLUSIONS

The research in this thesis increased the capabilities of multimode fibre endoscopes by CARS imaging. It led to the implementation of SHG imaging (which is not part of this thesis but was demonstrated in [45] using the imaging system developed in this thesis). These techniques, together with TPEF (also shown here) form a basis for optical biopsies. Implementing them through the miniature multimode fibre thus could lead towards diagnosing tumours deep in tissue with minimal damage.

While the presented work showed that it is feasible to perform non-linear imaging techniques, including label-free imaging, through a multimode fibre, there is still a long way towards a practical implementation for, for example, clinical applications. In addition, some issues with the current implementation remained unsolved. Thus, the first step of follow-up research should be to address the two issues with CARS imaging with a femtosecond laser that have not been fully explained here, namely, the exact source of the background signal generated in the fibre and the reduced spectral resolution of CARS compared to a microscope. While the background was suppressed sufficiently to allow imaging, narrowing down its exact source would require performing additional measurements using the picosecond laser system and using a femtosecond laser system at different wavelengths (neither of which was possible at the time of discovering the background) as well as another type of graded-index fibres. As for the reduced spectral resolution, this would require a more in-depth characterisation of the pulses in the sample plane.

Another technological progress could be made in developing the multimode fibre probes. Tissue imaging would greatly benefit from using the side-view probes, now commonly used within ISI Complex Photonics group for linear imaging in-vivo. In addition, the probes should ideally have a larger numerical aperture. While the highest numerical aperture of currently commercially available graded-index fibres is about 0.30, advances in manufacturing fibres and graded-index lenses could potentially allow higher values. A dimensionally more suitable pair of step-index and graded-index fibre should be found if it is necessary to continue using the composite probe for background suppression.

A substantial step towards applications would be to implement the non-linear techniques using a digital micromirror device (DMD) as a spatial light modulator, used commonly for linear imaging through multimode fibres. DMDs offer about two orders of magnitude higher frame rates than liquid-crystal spatial light modulators. Their low efficiency (caused by a binary amplitude modulation) and high dispersion makes them challenging to use with pulsed light sources for non-linear imaging techniques, where high excitation powers and proper control over the dispersion are necessary. This could, however, change soon when phase-modulating micromirror devices (PLMs) become commercially available. Currently, these devices from Texas Instruments are only available as samples. Combining a PLM with a higher-power laser system would allow non-linear imaging with frame rates more suitable for in-vivo applications.

These steps would then open the possibilities for biological applications. Thus, the next step would be testing tissue imaging, including diagnosing tumorous tissue or other pathological states. Showing that such determination could be done in-vivo would set the scene for possible clinical applications of the endoscope.

# References

- [1] GU, Min, Xiaosong GAN, Aernout KISTEMAN and Ming Gun XU. Comparison of Penetration Depth between Two-Photon Excitation and Single-Photon Excitation in Imaging through Turbid Tissue Media. *Applied Physics Letters*. 2000, vol. 77, no. 10, pp. 1551–1553. ISSN 1077-3118. Available from: doi:10.1063/1.1308059.
- [2] DENG, Xiaoyuan and Min GU. Penetration Depth of Single-, Two-, and Three-Photon Fluorescence Microscopic Imaging through Human Cortex Structures: Monte Carlo Simulation. *Applied Optics*. 2003, vol. 42, no. 16, pp. 3321–3329. ISSN 1539-4522. Available from: doi:10.1364/AO.42.003321.
- [3] GIGAN, Sylvain, Ori KATZ, Hilton B. de AGUIAR, Esben Ravn ANDRESEN, Alexandre AUBRY, Jacopo BERTOLOTTI, Emmanuel BOSSY, Dorian BOUCHET, Joshua BRAKE, Sophie BRASSELET, Yaron BROMBERG, Hui CAO, Thomas CHAIGNE, Zhongtao CHENG, Wonshik CHOI, Tomáš ČIŽMÁR, Meng CUI, Vincent R. CURTIS, Hugo DEFIENNE, Matthias HOFER, Ryoichi HORISAKI, Roarke HORSTMAYER, Na JI, Aaron K. LAVIOLETTE, Jerome MERTZ, Christophe MOSER, Allard P. MOSK, Nicolas C. PÉGARD, Rafael PIESTUN, Sébastien POPOFF, David B. PHILLIPS, Demetri PSALTIS, Babak RAHMANI, Hervé RIGNEAULT, Stefan ROTTER, Lei TIAN, Ivo M. VELLEKOOP, Laura WALLER, Lihong WANG, Timothy WEBER, Sheng XIAO, Chris XU, Alexey YAMILOV, Changhui YANG and Hasan YILMAZ. Roadmap on Wavefront Shaping and Deep Imaging in Complex Media. *Journal of Physics: Photonics*. 2022, vol. 4, no. 4, pp. 042501. ISSN 2515-7647. Available from: doi:10.1088/2515-7647/ac76f9.
- [4] FLUSBERG, Benjamin A., Eric D. COCKER, Wibool PIYAWATTANAMETHA, Juergen C. JUNG, Eunice L. M. CHEUNG and Mark J. SCHNITZER. Fiber-Optic Fluorescence Imaging. *Nature Methods*. 2005, vol. 2, no. 12, pp. 941–950. ISSN 1548-7105. Available from: doi:10.1038/nmeth820.
- [5] ORTH, Antony, Martin PLÖSCHNER, Emma. R. WILSON, Ivan S. MAKSYMOW and Brant C. GIBSON. Optical Fiber Bundles: Ultra-slim Light Field Imaging Probes. *Science Advances*. 2019, vol. 5, no. 4, pp. eaav1555. ISSN 2375-2548. Available from: doi:10.1126/sciadv.aav1555.
- [6] FLUSBERG, Benjamin A., Juergen C. JUNG, Eric D. COCKER, Erik P. ANDERSON and Mark J. SCHNITZER. In Vivo Brain Imaging Using a Portable 39 Gram Two-Photon Fluorescence Microendoscope. *Optics Letters*. 2005, vol. 30, no. 17, pp. 2272–2274. ISSN 1539-4794. Available from: doi:10.1364/OL.30.002272.
- [7] GHOSH, Kunal K., Laurie D. BURNS, Eric D. COCKER, Axel NIMMERJAHN, Yaniv ZIV, Abbas El. GAMAL and Mark J. SCHNITZER. Miniaturized Integration of a Fluorescence Microscope. *Nature Methods*. 2011, vol. 8, no. 10, pp. 871–878. ISSN 1548-7105. Available from: doi:10.1038/nmeth.1694.

## REFERENCES

- [8] WANG, Taejun, Qingyun LI, Peng XIAO, Jinhyo AHN, Young Eun KIM, Young-rong PARK, Minjun KIM, Miyeoun SONG, Euiheon CHUNG, Wan Kyun CHUNG, G-One AHN, Sungjee KIM, Pilhan KIM, Seung-Jae MYUNG and Ki Hean KIM. Gradient Index Lens Based Combined Two-Photon Microscopy and Optical Coherence Tomography. *Optics Express*. 2014, vol. 22, no. 11, pp. 12962–12970. ISSN 1094-4087. Available from: doi:10.1364/OE.22.012962.
- [9] BARRETTO, Robert P. J., Tony H. KO, Juergen C. JUNG, Tammy J. WANG, George CAPPS, Allison C. WATERS, Yaniv ZIV, Alessio ATTARDO, Lawrence RECHT and Mark J. SCHNITZER. Time-Lapse Imaging of Disease Progression in Deep Brain Areas Using Fluorescence Microendoscopy. *Nature Medicine*. 2011, vol. 17, no. 2, pp. 223–228. ISSN 1078-8956. Available from: doi:10.1038/nm.2292.
- [10] ČIŽMÁR, Tomáš and Kishan DHOLAKIA. Shaping the Light Transmission through a Multimode Optical Fibre: Complex Transformation Analysis and Applications in Biophotonics. *Optics Express*. 2011, vol. 19, no. 20, pp. 18871–18884. ISSN 1094-4087. Available from: doi:10.1364/OE.19.018871.
- [11] DI LEONARDO, Roberto and Silvio BIANCHI. Hologram Transmission through Multi-Mode Optical Fibers. *Optics Express*. 2011, vol. 19, no. 1, pp. 247–254. ISSN 1094-4087. Available from: doi:10.1364/OE.19.000247.
- [12] TURTAEV, Sergey, Ivo T. LEITE, Tristan ALTWEGG-BOUSSAC, Janelle M. P. PAKAN, Nathalie L. ROCHEFORT and Tomáš ČIŽMÁR. High-Fidelity Multimode Fibre-Based Endoscopy for Deep Brain in Vivo Imaging. *Light: Science & Applications*. 2018, vol. 7, no. 92. ISSN 2047-7538. Available from: doi:10.1038/s41377-018-0094-x.
- [13] VASQUEZ-LOPEZ, Sebastian A., Raphaël TURCOTTE, Vadim KOREN, Martin PLÖSCHNER, Zahid PADAMSEY, Martin J. BOOTH, Tomáš ČIŽMÁR and Nigel J. EMPTAGE. Subcellular Spatial Resolution Achieved for Deep-Brain Imaging in Vivo Using a Minimally Invasive Multimode Fiber. *Light: Science & Applications*. 2018, vol. 7, no. 110. ISSN 2047-7538. Available from: doi:10.1038/s41377-018-0111-0.
- [14] STIBŮREK, Miroslav, Petra ONDRÁČKOVÁ, Tereza TUČKOVÁ, Sergey TURTAEV, Martin ŠILER, Tomáš PIKÁLEK, Petr JÁKL, André GOMES, Jana KREJČÍ, Petra KOLBÁBKOVÁ, Hana UHLÍŘOVÁ and Tomáš ČIŽMÁR. 110  $\mu\text{m}$  Thin Endo-Microscope for Deep-Brain in Vivo Observations of Neuronal Connectivity, Activity and Blood Flow Dynamics. *Nature Communications*. 2023, vol. 14, pp. 1897. ISSN 2041-1723. Available from: doi:10.1038/s41467-023-36889-z.
- [15] MORALES-DELGADO, Edgar E., Demetri PSALTIS and Christophe MOSER. Two-Photon Imaging through a Multimode Fiber. *Optics Express*. 2015, vol. 23, no. 25, pp. 32158–32170. ISSN 1094-4087. Available from: doi:10.1364/OE.23.032158.
- [16] SIVANKUTTY, Siddharth, Esben Ravn ANDRESEN, Rosa COSSART, Géraud BOUWMANS, Serge MONNERET and Hervé RIGNEAULT. Ultra-Thin Rigid Endoscope: Two-Photon Imaging through a Graded-Index Multi-Mode Fiber. *Optics Express*. 2016, vol. 24, no. 2, pp. 825–841. ISSN 1094-4087. Available from: doi:10.1364/OE.24.000825.

- [17] KAKKAVA, Eirini, Marilisa ROMITO, Donald B. CONKEY, Damien LOTERIE, Konstantina M. STANKOVIC, Christophe MOSER and Demetri PSALTIS. Selective Femtosecond Laser Ablation via Two-Photon Fluorescence Imaging through a Multimode Fiber. *Biomedical Optics Express*. 2019, vol. 10, no. 2, pp. 423–433. ISSN 2156-7085. Available from: doi:10.1364/BOE.10.000423.
- [18] BEGLEY, R. F., A. B. HARVEY and R. L. BYER. Coherent anti-Stokes Raman Spectroscopy. *Applied Physics Letters*. 1974, vol. 25, no. 7, pp. 387–390. ISSN 1077-3118. Available from: doi:10.1063/1.1655519.
- [19] MEYER, Tobias, Mario CHEMNITZ, Martin BAUMGARTL, Thomas GOTTSCHALL, Torbjörn PASCHER, Christian MATTHÄUS, Bernd F. M. ROMEIKE, Bernhard R. BREHM, Jens LIMPET, Andreas TÜNNERMANN, Michael SCHMITT, Benjamin DIETZEK and Jürgen POPP. Expanding Multimodal Microscopy by High Spectral Resolution Coherent Anti-Stokes Raman Scattering Imaging for Clinical Disease Diagnostics. *Analytical Chemistry*. 2013, vol. 85, no. 14, pp. 6703–6715. ISSN 0003-2700. Available from: doi:10.1021/ac400570w.
- [20] PIKÁLEK, Tomáš, Johanna TRÄGÅRDH, Stephen SIMPSON and Tomáš ČIŽMÁR. Wavelength Dependent Characterization of a Multimode Fibre Endoscope. *Optics Express*. 2019, vol. 27, no. 20, pp. 28239–28253. ISSN 1094-4087. Available from: doi:10.1364/OE.27.028239.
- [21] TRÄGÅRDH, Johanna, Tomáš PIKÁLEK, Mojmír ŠERÝ, Tobias MEYER, Jürgen POPP and Tomáš ČIŽMÁR. Label-Free CARS Microscopy through a Multimode Fibre Endoscope. *Optics Express*. 2019, vol. 27, no. 21, pp. 30055–30066. ISSN 1094-4087. Available from: doi:10.1364/OE.27.030055.
- [22] PIKÁLEK, Tomáš, Miroslav STIBŮREK, Stephen SIMPSON, Tomáš ČIŽMÁR and Johanna TRÄGÅRDH. Suppression of the Non-Linear Background in a Multimode Fibre CARS Endoscope. *Biomedical Optics Express*. 2022, vol. 13, no. 2, pp. 862–864. ISSN 2156-7085. Available from: doi:10.1364/BOE.450375.
- [23] TURCOTTE, Raphaël, Carla C. SCHMIDT, Martin J. BOOTH and Nigel J. EMP- TAGE. Volumetric Two-Photon Fluorescence Imaging of Live Neurons Using a Multimode Optical Fiber. *Optics Letters*. 2020, vol. 45, no. 24, pp. 6599–6602. ISSN 1539-4794. Available from: doi:10.1364/OL.409464.
- [24] LEACH, Jonathan, Graham M. GIBSON, Miles J. PADGETT, Elric ESPOSITO, Gail MCCONNELL, Amanda J. WRIGHT and John M. GIRKIN. Generation of Achromatic Bessel Beams Using a Compensated Spatial Light Modulator. *Optics Express*. 2006, vol. 14, no. 12, pp. 5581–5587. ISSN 1094-4087. Available from: doi:10.1364/OE.14.005581.
- [25] EVERALL, Neil J. Confocal Raman Microscopy: Performance, Pitfalls, and Best Practice: Invited Lecture at the Symposium “50 Years of SAS: Looking to the Future with Vibrational Spectroscopy” at Pittcon 2008, New Orleans, Louisiana. *Applied Spectroscopy*. 2009, vol. 63, no. 9, pp. 245A–262A. ISSN 1943-3530. Available from: doi:10.1366/000370209789379196.
- [26] CHENG, Ji-Xin and X. Sunney XIE. Coherent Anti-Stokes Raman Scattering Microscopy: Instrumentation, Theory, and Applications. *The Journal of Physical Chemistry B*. 2004, vol. 108, no. 3, pp. 827–840. ISSN 1520-5207. Available from: doi:10.1021/jp035693v.

## REFERENCES

- [27] POTMA, Eric O. and X. Sunney XIE. CARS Microscopy for Biology and Medicine. *Optics and Photonics News*. 2004, vol. 15, no. 11, pp. 40–45. ISSN 1541-3721. Available from: doi:10.1364/OPN.15.11.000040.
- [28] LATKA, Ines, Sebastian DOCHOW, Christoph KRAFFT, Benjamin DIETZEK and Jürgen POPP. Fiber Optic Probes for Linear and Nonlinear Raman Applications – Current Trends and Future Development: Fiber Optic Raman Probes. *Laser & Photonics Reviews*. 2013, vol. 7, no. 5, pp. 698–731. ISSN 1863-8880. Available from: doi:10.1002/lpor.201200049.
- [29] EVANS, Conor L. and X. Sunney XIE. Coherent Anti-Stokes Raman Scattering Microscopy: Chemical Imaging for Biology and Medicine. *Annual Review of Analytical Chemistry*. 2008, vol. 1, no. 1, pp. 883–909. ISSN 1936-1335. Available from: doi:10.1146/annurev.anchem.1.031207.112754.
- [30] UCKERMANN, Ortrud, Roberta GALLI, Sandra TAMOSAITYTE, Elke LEIPNITZ, Kathrin D. GEIGER, Gabriele SCHACKERT, Edmund KOCH, Gerald STEINER and Matthias KIRSCH. Label-Free Delineation of Brain Tumors by Coherent Anti-Stokes Raman Scattering Microscopy in an Orthotopic Mouse Model and Human Glioblastoma. *PLoS ONE*. 2014, vol. 9, no. 9, pp. e107115. ISSN 1932-6203. Available from: doi:10.1371/journal.pone.0107115.
- [31] BOCKLITZ, Thomas W., Firas Subhi SALAH, Nadine VOGLER, Sandro HEUKE, Olga CHERNAVSKAIA, Carsten SCHMIDT, Maximilian J. WALDNER, Florian R. GRETEN, Rolf BRÄUER, Michael SCHMITT, Andreas STALLMACH, Iver PETERSEN and Jürgen POPP. Pseudo-HE Images Derived from CARS/T-PEF/SHG Multimodal Imaging in Combination with Raman-spectroscopy as a Pathological Screening Tool. *BMC Cancer*. 2016, vol. 16, pp. 534. ISSN 1471-2407. Available from: doi:10.1186/s12885-016-2520-x.
- [32] KRAFFT, Christoph, Iwan W. SCHIE, Tobias MEYER, Michael SCHMITT and Jürgen POPP. Developments in Spontaneous and Coherent Raman Scattering Microscopic Imaging for Biomedical Applications. *Chemical Society Reviews*. 2016, vol. 45, no. 7, pp. 1819–1849. ISSN 1460-4744. Available from: doi:10.1039/C5CS00564G.
- [33] HENRY, Francis P., Daniel CÔTÉ, Mark A. RANDOLPH, Esther A. Z. RUST, Robert W. REDMOND, Irene E. KOICHEVAR, Charles P. LIN and Jonathan M. WINOGRAD. Real-Time In Vivo Assessment of the Nerve Microenvironment with Coherent Anti-Stokes Raman Scattering Microscopy: *Plastic and Reconstructive Surgery*. 2009, vol. 123, pp. 123S–130S. ISSN 0032-1052. Available from: doi:10.1097/PRS.0b013e318191c5b8.
- [34] WELTE, Michael A. As the Fat Flies: The Dynamic Lipid Droplets of Drosophila Embryos. *Biochimica et Biophysica Acta*. 2015, vol. 1851, no. 9, pp. 1156–1185. ISSN 1388-1981. Available from: doi:10.1016/j.bbali.2015.04.002.
- [35] EVANS, Conor L., Eric O. POTMA, Mehron PUORIS’HAAG, Daniel COTE, Charles P. LIN and X. Sunney XIE. Chemical Imaging of Tissue in Vivo with Video-Rate Coherent Anti-Stokes Raman Scattering Microscopy. *Proceedings of the National Academy of Sciences*. 2005, vol. 102, no. 46, pp. 16807–16812. ISSN 0027-8424. Available from: doi:10.1073/pnas.0508282102.

- [36] MITTAL, Richa, Mihaela BALU, Petra WILDER-SMITH and Eric O. POTMA. Achromatic Miniature Lens System for Coherent Raman Scattering Microscopy. *Biomedical Optics Express*. 2013, vol. 4, no. 10, pp. 2196–2206. ISSN 2156-7085. Available from: doi:10.1364/BOE.4.002196.
- [37] ZIRAK, Peyman, Gregor MATZ, Bernhard MESSERSCHMIDT, Tobias MEYER, Michael SCHMITT, Jürgen POPP, Ortrud UCKERMANN, Roberta GALLI, Matthias KIRSCH, Martin Josef WINTERHALDER and Andreas ZUMBUSCH. Invited Article: A Rigid Coherent Anti-Stokes Raman Scattering Endoscope with High Resolution and a Large Field of View. *APL Photonics*. 2018, vol. 3, no. 9, pp. 092409. ISSN 2378-0967. Available from: doi:10.1063/1.5027182.
- [38] PSHENAY-SEVERIN, Ekaterina, Hyeonsoo BAE, Karl REICHWALD, Gregor MATZ, Jörg BIERLICH, Jens KOBELKE, Adrian LORENZ, Anka SCHWUCHOW, Tobias MEYER-ZEDLER, Michael SCHMITT, Bernhard MESSERSCHMIDT and Jürgen POPP. Multimodal Nonlinear Endomicroscopic Imaging Probe Using a Double-Core Double-Clad Fiber and Focus-Combining Micro-Optical Concept. *Light: Science & Applications*. 2021, vol. 10, no. 207. ISSN 2047-7538. Available from: doi:10.1038/s41377-021-00648-w.
- [39] LUKIC, Aleksandar, Sebastian DOCHOW, Hyeonsoo BAE, Gregor MATZ, Ines LATKA, Bernhard MESSERSCHMIDT, Michael SCHMITT and Jürgen POPP. Endoscopic Fiber Probe for Nonlinear Spectroscopic Imaging. *Optica*. 2017, vol. 4, no. 5, pp. 496–501. ISSN 2334-2536. Available from: doi:10.1364/OPTICA.4.000496.
- [40] SAAR, Brian G., Richard S. JOHNSTON, Christian W. FREUDIGER, X. Sunney XIE and Eric J. SEIBEL. Coherent Raman Scanning Fiber Endoscopy. *Optics Letters*. 2011, vol. 36, no. 13, pp. 2396–2398. ISSN 1539-4794. Available from: doi:10.1364/OL.36.002396.
- [41] HELLERER, Thomas, Annika M.K. ENEJDER and Andreas ZUMBUSCH. Spectral Focusing: High Spectral Resolution Spectroscopy with Broad-Bandwidth Laser Pulses. *Applied Physics Letters*. 2004, vol. 85, no. 1, pp. 25–27. ISSN 1077-3118. Available from: doi:10.1063/1.1768312.
- [42] BRUSTLEIN, Sophie, Pascal BERTO, Richard HOSTEIN, Patrick FERRAND, Cyrille BILLAUDEAU, Didier MARGUET, Alistair MUIR, Jonathan KNIGHT and Hervé RIGNEAULT. Double-Clad Hollow Core Photonic Crystal Fiber for Coherent Raman Endoscope. *Optics Express*. 2011, vol. 19, no. 13, pp. 12562–12568. ISSN 1094-4087. Available from: doi:10.1364/OE.19.012562.
- [43] LU, Fa-Ke, Srinjan BASU, Vivien IGRAS, Mai P. HOANG, Minbiao JI, Dan FU, Gary R. HOLTOM, Victor A. NEEL, Christian W. FREUDIGER, David E. FISHER and X. Sunney XIE. Label-Free DNA Imaging in Vivo with Stimulated Raman Scattering Microscopy. *Proceedings of the National Academy of Sciences*. 2015, vol. 112, no. 37, pp. 11624–11629. ISSN 0027-8424. Available from: doi:10.1073/pnas.1515121112.
- [44] DEVAUD, Louisiane, Marc GUILLON, Ivan GUSACHENKO and Sylvain GIGAN. Chromato-Axial Memory Effect in Step Index Multimode Fibers. *APL Photonics*. 2021, vol. 6, no. 12. ISSN 2378-0967. Available from: doi:10.1063/5.0067892.

## REFERENCES

- [45] CIFUENTES, Angel, Tomáš PIKÁLEK, Petra ONDRÁČKOVÁ, Rodrigo AMEZCUA-CORREA, José Enrique ANTONIO-LOPEZ, Tomáš ČIŽMÁR and Johanna TRÄGÅRDH. Polarization-Resolved Second-Harmonic Generation Imaging through a Multimode Fiber. *Optica*. 2021, vol. 8, no. 8, pp. 1065–1074. ISSN 2334-2536. Available from: doi:10.1364/OPTICA.430295.
- [46] SILVEIRA, Beatriz M., Tomáš PIKÁLEK, Miroslav STIBŮREK, Petra ONDRÁČKOVÁ, Petr JÁKL, Ivo T. LEITE and Tomáš ČIŽMÁR. Side-View Holographic Endomicroscopy via a Custom-Terminated Multimode Fibre. *Optics Express*. 2021, vol. 29, no. 15, pp. 23083–23095. ISSN 1094-4087. Available from: doi:10.1364/OE.426235.



# Tomáš Pikálek

---

## Curriculum vitae

### Personal data

Name Ing. Tomáš Pikálek  
Date of birth 3rd November 1991  
Nationality Czech

### Work experience

2016–present **Institute of Scientific Instruments of the CAS**, Brno  
Ph.D. student  
Group of Complex Photonics (2018–present)  
Group of Coherent Lasers and Interferometry (2016–2019)

### Education

2016–present **Doctoral Study**  
Physical Engineering  
Faculty of Mechanical Engineering, Brno University of Technology  
Topic: *Multiphoton and non-linear Raman microscopy through a multimode fibre*  
Supervisor: prof. Mgr. Tomáš Čížmár, Ph.D. (Institute of Scientific Instruments of the CAS)

2014–2016 **Master's Degree Programme**  
Physical Engineering and Nanotechnology  
Faculty of Mechanical Engineering, Brno University of Technology  
Master's thesis: *Analysis and verification of air refractive index measurement method for laser interferometry*  
Supervisor: Ing. Zdeněk Buchta, Ph.D. (Institute of Scientific Instruments of the CAS)

2011–2014 **Bachelor's Degree Programme**  
Physical Engineering and Nanotechnology  
Faculty of Mechanical Engineering, Brno University of Technology  
Bachelor's thesis: *Surface analysis using low-coherence interferometry*  
Supervisor: Ing. Zdeněk Buchta, Ph.D. (Institute of Scientific Instruments of the CAS)

### Internships

2015 **University of Natural Resources and Life Sciences**, Vienna, Austria  
Institute for Biologically Inspired Materials, Department of Nanobiotechnology  
6 months Erasmus stay  
Projects: *Preparation of flexible strings of colloidal particles. Measurement of dipole-dipole interaction between colloidal particles by means of digital video microscopy.*  
Supervisor: Dr. Peter van Oostrum

## Scholarships

2011–2014 **Gifted Students Support Programme of the South Moravian Region**  
South Moravian Centre for International Mobility, Brno

## Awards and competitions

2017 **Werner von Siemens Excellence Award**

The best diploma thesis

*Analysis and verification of air refractive index measurement method for laser interferometry*

2016 **Rector's Award**

Brno University of Technology Rector's Award for excellent results in Master study programme

2012 **Werner von Siemens Excellence Award**

The most important result of the development/innovation

*Method of non-contact gauge block calibration* (Institute of Scientific Instruments of the CAS)

## Language proficiency

Czech Native speaker

English Level C1

## Computer skills

Engineering Autodesk Inventor, software for FDM 3D printers

Scientific MATLAB, LabVIEW, L<sup>A</sup>T<sub>E</sub>X, gnuplot